

# Time-Series Forecasting via Topological Information Supervised Framework with Efficient Topological Feature Learning

ZiXin Lin, Nur Fariha Syaqina Zulkepli\*

*School of Mathematical Sciences, Universiti Sains Malaysia, 11800, Penang*

## Abstract

Topological Data Analysis (TDA) has emerged as a powerful tool for extracting meaningful features from complex data structures, driving significant advancements in fields such as neuroscience, biology, machine learning, and financial modeling. Despite its success, the integration of TDA with time-series prediction remains underexplored due to three primary challenges: the limited utilization of temporal dependencies within topological features, computational bottlenecks associated with persistent homology, and the deterministic nature of TDA pipelines restricting generalized feature learning. This study addresses these challenges by proposing the Topological Information Supervised (TIS) Prediction framework, which leverages neural networks and Conditional Generative Adversarial Networks (CGANs) to generate synthetic topological features, preserving their distribution while significantly reducing computational time. We propose a novel training strategy that integrates topological consistency loss to improve the predictive accuracy of deep learning models. Specifically, we introduce two state-of-the-art models, TIS-BiGRU and TIS-Informer, designed to capture short-term and long-term temporal dependencies, respectively. Comparative experimental results demonstrate the superior performance of TIS models over conventional predictors, validating the effectiveness of integrating topological information. This work not only advances TDA-based time-series prediction but also opens new avenues for utilizing topological features in deep learning architectures.

**Keywords:** Computational Topology, Conditional Generative Adversarial Network, Forecasting, Persistent Homology, Informer

## 1 Introduction

In recent years, Topological Data Analysis (TDA) has gained significant attention for its powerful ability to extract meaningful features from complex data, leading to successful applications across diverse fields. In neuroscience and biology, TDA has been used to analyze brain connectivity patterns [1, 2], complex cell structures [3, 4], cancer detection [5, 6], and disease diagnosis [7]. By providing insights into the shape and structure of high-dimensional genomic data, TDA offers a unique perspective that traditional methods often overlook. In machine learning applications, TDA has enhanced model performance for classification and clustering tasks by capturing topological features that conventional approaches might miss. Its applications span a wide range of areas, including pollution pattern analysis [8], sleep-wake classification [9], image classification [10], sea level pattern analysis [11], material internal structure analysis [12], geographical information extraction [13], medium-range order in glass structures [14], and object recognition in cluttered environments [15]. Furthermore, TDA has proven valuable in financial modeling, where it is utilized to detect market trends and anomalies [16, 17, 18, 19, 20, 21]. Its robustness and capacity to provide interpretable insights from noisy and high-dimensional datasets have driven its growing popularity, underscoring its versatility and effectiveness in addressing modern data science challenges [22, 23]. These diverse applications highlight TDA's potential

as a transformative tool across scientific disciplines, paving the way for more innovative and effective data analysis solutions.

However, the integration of TDA with time-series prediction remains relatively unexplored. This can be attributed to several challenges. First, there is a prevailing notion that TDA, known for quantifying structural information within data, is better suited for pattern recognition or cluster analysis than for time-series prediction [24, 6]. As a result, most studies leveraging persistent homology, a fundamental tool in TDA, primarily extract topological features as input variables for learning models (see more works in [25, 26, 27, 28, 29, 30, 31, 32, 33]). This approach, however, often overlooks the potential of utilizing the temporal dependencies embedded in the topological features of time-series data, which could guide models to learn more optimal parameters within the parameter space. Additionally, for long-sequence time-series, the construction of complex persistent homology landscapes becomes a significant computational bottleneck, impeding efficient learning and predictive accuracy, as we will see in Section 6.1. Although libraries such as **Giotto-TDA** [34], **Ripser** [35], **GUDHI**, **Perseus** [36], or **Scikit-TDA** [37] provide efficient tools for computing persistent homology, they are predominantly based on CPU computation. While leveraging GPU acceleration technique, such as **CuPy** [38], can potentially enhance computational efficiency, it often necessitates substantial modifications to the existing libraries' architectures, posing challenges in implementation and integration. Third, the computation process, which typically involves reconstructing the time-series into phase space followed by the construction of complex persistent homology, is inherently deterministic. This end-to-end pipeline generates highly specific topological features as output [39], limiting the model's ability to learn flexible and generalized representations. Consequently, the rigidity of this deterministic approach restricts the adaptability of the learned features, potentially impacting the model's predictive accuracy and generalization to unseen data [40].

Centered around the relatively unexplored integration of TDA with time-series prediction and the associated challenges, this study aims to address and answer the following questions:

1. How can temporal dependencies within topological features be effectively leveraged to enhance time-series prediction?
2. What strategies can be employed to overcome the computational bottlenecks associated with constructing persistent homology landscapes for long-sequence time-series data?
3. How can the deterministic nature of the persistent homology pipeline be addressed to enable more flexible and generalized feature learning?
4. What is the impact of integrating TDA with state-of-the-art deep learning models on time-series prediction accuracy and generalization?

A formal formulation of the problems presented above can be found in Section 3. In response to these questions and as the main contributions of this work, we have taken several steps:

1. To overcome the computational bottleneck, the first step involves training a neural network,  $\text{Net}_\theta$ , to generate synthetic topological features that closely resemble real topological features obtained through TDA computation. To ensure the synthetic features share a similar distribution with the real features, Generative Adversarial Network (GAN) [41] frameworks were utilized to effectively learn the underlying distribution of the real topological features. Details can be found in Sections 3 and 4.
2. To integrate topological features into the prediction task and enhance time-series forecasting accuracy, we propose the Topological Information Supervised (TIS) Prediction framework, built on the pre-trained neural network,  $\text{Net}_\theta$ . The extracted topological features are embedded by a Topological Embedder into a suitable space and combined with

the original historical data, forming an enriched representation that is fed into the predictor. Additionally, we introduce a novel training strategy where the model is trained using a combined loss function, consisting of prediction loss and topological loss, to ensure consistency in high-level topological patterns and internal dynamics. We developed three frameworks of Conditional GAN (CGAN), including recurrent neural network [42] CGAN, reconstructor-guided CGAN, and stacked CGAN [43]. Details can be found in Sections 3 and 4.

3. We propose two novel models, TIS-Bidirectional Gated Recurrent Unit (BiGRU) [44] and TIS-Informer [45], which integrate topological information and topological consistency loss functions with state-of-the-art deep learning architectures. TIS-BiGRU is designed for short-term prediction (6h–36h), leveraging bidirectional gated recurrent units to effectively capture temporal dependencies. In contrast, TIS-Informer is optimized for long-term prediction (48h–336h) by utilizing an efficient attention mechanism that handles long-sequence dependencies. Experimental results demonstrate that the TIS models consistently outperform conventional predictors that do not incorporate and are not supervised by topological information, achieving superior performance across predefined metrics. Details can be found in Section 5.
4. We conducted a comprehensive study to explore the computation time required for inference, highlighting the significant speed-up effect achieved through our proposed approach. Additionally, we investigated how different types of simplicial complexes impact forecasting accuracy, revealing the influence of topological structures on model performance. Furthermore, we examined the role of the GAN framework in enabling the models to effectively capture the underlying distributions of topological features. Detailed empirical results supporting these findings are provided in Section 6.

The rest of this paper is structured as follows: In Section 2, we review the preliminaries that provide the foundational basis for this study. In Section 3, we formally define the problems addressed in this research. Section 4 details the proposed methods, including model frameworks, architectures, training procedures, and other technical aspects. In Section 5, we present the experimental results demonstrating the impact of incorporating topological information into the predictive models. In Section 6, we present an ablation study of key considerations, including computational times, the role of GANs in learning topological features, and the selection of essential hyperparameters. In Section 7, we discuss the limitations of this study and potential directions for future research. Finally, Section 8 provides the conclusion of this study.

## 2 Preliminaries

### 2.1 Topology data analysis

#### 2.1.1 Persistent homology

An  $n$ -simplex, denoted by  $\sigma^n$ , is defined as the smallest convex set that contains  $n + 1$  points in general position. The formal definition is given below.

**Definition 1** (Simplex [6]). *An  $n$ -simplex  $\sigma^n$  is the convex hull of  $n + 1$  affinely independent points  $v_0, v_1, \dots, v_n \in \mathbb{R}^d$ . Any point  $p \in \sigma^n$  can be expressed as a convex combination of these vertices:*

$$p = \sum_{i=0}^n \lambda_i v_i, \quad \text{where } \lambda_i \geq 0 \quad \text{and} \quad \sum_{i=0}^n \lambda_i = 1. \quad (1)$$

A simplicial complex, is a collection of simplices that satisfies certain conditions of adjacency and intersection.

1. If a simplex is in the complex, then all of its faces (lower-dimensional parts) are also included.
2. Any two simplices in the complex either do not overlap at all, or they intersect along a shared face.

For  $X = \{x_1, x_2, \dots, x_n\}$  in a metric space  $(M, d)$ , where  $d$  is a distance function on  $M$ . In topological data analysis, several types of simplicial complexes are employed to analyze the shape of data. One such construction is the Vietoris-Rips complex:

**Definition 2** (Vietoris-Rips Complex [46]). *The Vietoris-Rips complex  $R_\epsilon(X)$  at a given scale  $\epsilon$  is formed as follows: a finite set of points  $\{x_i, x_j\}$  spans a 1-simplex in  $R_\epsilon(X)$  if and only if*

$$d(x_i, x_j) \leq \epsilon. \quad (2)$$

*More generally, for each  $\epsilon$ , the complex  $R_\epsilon(X)$  includes all simplices whose vertices are pairwise within distance  $\epsilon$ , with higher-dimensional simplices added accordingly (e.g., triangles, tetrahedra).*

**Definition 3** (Weighted Vietoris-Rips complex [46] with DTM [47] weights). *Weighted Vietoris-Rips complex at scale  $\epsilon$  with Distance-to-Measure (DTM) weights is a simplicial complex where:*

$$\text{Simplex}\{x_i, x_j\} \in R_\epsilon^w(X) \quad \text{if and only if} \quad d(x_i, x_j) \leq \epsilon (w(x_i) + w(x_j)), \quad (3)$$

where  $w(x)$  is the weight function given by the DTM:

$$w(x) = DTM(x, K) = 2 \left( \frac{1}{K+1} \sum_{k=1}^K d(x, x_{(k)})^2 \right)^{\frac{1}{2}}, \quad (4)$$

where  $x_{(k)}$  is the  $k$ -th nearest neighbor of  $x$  and  $K$  is the number of nearest neighbors to include.

**Definition 4** (Cubical Complex [48]). *A cubical complex  $C$  is a set of cubes where:*

$$\text{Cube } Q = [a_1, b_1] \times [a_2, b_2] \times \dots \times [a_n, b_n], \quad (5)$$

where each interval is either a point  $a_i = b_i$  or a unit interval  $[a_i, b_i] \subset \mathbb{R}$ . A  $k$ -dimensional cube is defined as the product of  $k$  unit intervals and  $n - k$  points.  $C$  is a cubical complex if it satisfies the following conditions:

1. If a cube  $Q$  belongs to  $C$ , then all its faces also belong to  $C$ .
2. If two cubes intersect, then their intersection is a face of both.

**Definition 5** (Cech complex [49]). *For a collection of points, the Cech complex is defined as:*

$$\mathcal{C}_\epsilon(X) = \left\{ \sigma \subset X \mid \bigcap_{x \in \sigma} B_\epsilon(x) \neq \emptyset \right\}, \quad (6)$$

where  $B_\epsilon(x)$  is the Euclidean ball centered at point  $x$  with radius  $\epsilon$ .

The boundary of a simplex is the set of its faces, which are simplices of lower dimensions. The boundary operator  $\partial\sigma^n$  is a formal sum of the faces of a simplex  $\sigma^n$ .

**Definition 6** (Boundary of a Simplex [6]). *For an  $n$ -simplex  $\sigma^n = [v_0, v_1, \dots, v_n]$ , the boundary of  $\sigma^n$ , denoted  $\partial\sigma^n$ , is the sum of all its  $(n - 1)$ -dimensional faces:*

$$\partial\sigma^n = \sum_{i=0}^n (-1)^i [v_0, \dots, \hat{v}_i, \dots, v_n], \quad (7)$$

where  $\hat{v}_i$  denotes that the vertex  $v_i$  is omitted from the face.

Formally, a filtration  $\mathcal{F}$  of a simplicial complex  $K$  is defined as a sequence of nested sub-complexes indexed by a non-decreasing scale parameter  $\epsilon$ :

$$\mathcal{F} : \emptyset = K_0 \hookrightarrow K_{\epsilon_1} \hookrightarrow \cdots \hookrightarrow K_{\epsilon_n} = K, \quad (8)$$

where  $\epsilon_i < \epsilon_j$  for  $i < j$ . Such a filtration allows us to track the birth and persistence of topological features across scales. To analyze the topological structure at each stage of this filtration, we use homology theory. A simplicial complex is composed of basic building blocks called simplices. Given a simplicial complex  $K$ , the algebraic structure of its homology is studied using chain groups, cycles, and boundaries. Let  $\mathbb{Z}_R$  be a module over a ring  $R$ . A  $p$ -chain is:

$$C_p = \left\{ c_p \left| c_p = \sum_{i=1}^{m_p} \alpha_i \sigma_i^p, \alpha_i \in \mathbb{Z}_R \right. \right\}, \quad (9)$$

where  $m_p$  is the number of  $p$ -simplices in the complex, and  $\sigma_i^p$  denotes a basis  $p$ -simplex. The boundary operator  $\partial_k$  maps  $k$ -chains to  $(k-1)$ -chains, allowing us to define cycles and boundaries [22] as follows:

$$\text{Ker}(\partial_k) = \{c_k \in C_k \mid \partial_k(c_k) = 0\}, \quad (10)$$

$$\text{Im}(\partial_{k+1}) = \{c_k \in C_k \mid \exists c_{k+1} \in C_{k+1}, \partial_{k+1}(c_{k+1}) = c_k\}. \quad (11)$$

The  $k$ -th homology group is the quotient group [22]:

$$H_k(K) = \frac{\text{Ker}(\partial_k)}{\text{Im}(\partial_{k+1})}. \quad (12)$$

The rank of  $H_k(K)$  is called the  $k$ -th Betti number and reflects the number of independent  $k$ -dimensional topological features [22]. Tracking these features across the filtration yields a sequence of homology groups:

$$0 \rightarrow \cdots \rightarrow H_p(K_{\epsilon_i}) \xrightarrow{h_p^{i,j}} \cdots \rightarrow H_p(K_{\epsilon_j}) \rightarrow \cdots \rightarrow H_p(K_{\epsilon_n}), \quad (13)$$

where  $h_p^{i,j}$  is the map induced by inclusion, carrying homology classes from one stage to another.

## 2.2 Topological Features Engineering

### 2.2.1 Persistent diagram

A *persistent diagram* [50] is a tool used to visualize the birth and death of topological features such as connected components, loops, and voids during the filtration process. It is a collection of points  $(b_i, d_i) \in \mathbb{R}^2$ , where each point represents a topological feature:

- $b_i$  is the birth time (the scale at which the feature appears),
- $d_i$  is the death time (the scale at which the feature disappears).

The points  $(b_i, d_i)$  are arranged in a diagram, where the x-axis represents the birth times, and the y-axis represents the death times. For a feature to persist, it is expected  $d_i > b_i$ .

**Definition 7** (Persistence Diagram). *Given a filtration  $\{K_\epsilon\}$  of a simplicial complex, the persistence diagram is a multiset  $\{(b_i, d_i)\}$  in which each pair represents the appearance and disappearance of a homological feature during the filtration process:*

$$\mathcal{D}_p = \{(b_i, d_i) \mid i \in I\}, \quad \text{where } 0 \leq b_i < d_i \leq \infty. \quad (14)$$

### 2.2.2 Persistent landscape

A *persistent landscape* [51] is a summary of the persistent diagram that allows for easier comparison and computation. Given a persistent diagram  $\mathcal{D}_p = \{(b_i, d_i)\}$ , we associate with each diagram a collection of functions  $\{L_k\}_{k \in \mathbb{N}}$ , where each  $L_k$  is a real-valued function defined on the interval  $[0, \infty)$ . Formally, the persistent landscape function is defined as follows.

**Definition 8** (Persistent Landscape). *Given a persistent diagram  $\mathcal{D}_p$ , the persistent landscape  $L_k$  is a function such that:*

$$L_k(x) = \sup_{(b_i, d_i) \in \mathcal{D}_p} (\max(0, k - |x - b_i|) + \max(0, k - |x - d_i|)). \quad (15)$$

Here,  $k$  controls the "level" of the landscape, with higher values of  $k$  capturing more persistent features.

These landscapes provide a way to capture the structure of the persistence diagram into a sequence of functions, which can then be used for various computational tasks, such as comparing persistence across different datasets.

### 2.2.3 Working flow to extract topological features

Given a time series  $X = \{x_1, x_2, \dots, x_L\}$ , where  $L$  indicates the sequence length, it is embedded into a higher-dimensional space using the Takens embedding method. Given a time delay  $\tau$  and an embedding dimension  $d$ , the embedded time series is given by:

$$\mathbf{x}_i = (x_i, x_{i+\tau}, \dots, x_{i+(d-1)\tau}), \quad (16)$$

where we assume  $x_i \in \mathbb{R}$ . The next step involves constructing a chosen type of complex from the embedded time series. A simplicial complex is created by considering the distances between the embedded points. In the experiments of this study, we employed the Vietoris-Rips complex, and a comparison of different types of complexes is presented in the Ablation Study Section.

Given the complex filtration, we construct a persistence diagram  $\mathcal{D} = \{(b_i, d_i)\}$ , and a persistence landscape  $\mathcal{L}$  on  $\mathcal{D}$ . The complete persistence landscape is a multi-layer function  $\ell_i(t)$  and formed by stacking these layers:

$$\mathcal{L} = \{\ell_1(t), \ell_2(t), \dots, \ell_p(t)\}. \quad (17)$$

From the persistence landscape, we extract several statistical features. These features include the **mean**, **variance**, and **median** of each layer  $\ell_i(t)$ . The mean of the  $i$ -th persistence landscape layer  $\ell_i(t)$  is computed as the average value of the layer over time  $t$ :

$$\text{mean}_i = \frac{1}{T} \sum_{t=1}^T \ell_i(t), \quad (18)$$

where  $T$  is the total number of time steps in the landscape. The variance of the  $i$ -th persistence landscape layer  $\ell_i(t)$  is computed as:

$$\text{variance}_i = \frac{1}{T} \sum_{t=1}^T (\ell_i(t) - \text{mean}_i)^2. \quad (19)$$

The median of the  $i$ -th persistence landscape layer  $\ell_i(t)$  is computed over all time steps:

$$\text{median}_i = \text{median}(\ell_i(t)), \quad \forall t \in [1, T]. \quad (20)$$

In addition to the statistics derived from the persistence landscape, we also compute the **max** and **mean** values of  $d_i - b_i$  for each homology dimension. For each dimension  $d$  and  $\mathcal{D} = \{(b_i, d_i)\}$ , we have:

$$\max_d = \max_i (d_i - b_i), \quad (21)$$

$$\text{mean}_d = \frac{1}{m} \sum_{i=1}^m (d_i - b_i), \quad (22)$$

where  $m$  is the total number of features in the persistence diagram for that homology dimension.

The final feature vector  $\mathbf{F}$  is obtained by concatenating the statistical features derived from both the persistence landscape and the persistence diagram. Specifically, the feature vector consists of:

- The **Number of Points** for birth-death pairs of each dimension in the persistence diagram  $\mathcal{D}$ ,
- The **max** and **mean** values of  $d_i - b_i$  for each homology dimension,
- The **mean**, **variance**, and **median** for each layer in the persistence landscape.

Thus, the final feature vector is:

$$\mathbf{F} = [\text{NumberOfPoints}(\mathcal{D}), \max\_mean\_features(\mathcal{D}), \text{mean}_i, \text{variance}_i, \text{median}_i]. \quad (23)$$

Such features have been found useful for encoding data dependency structures in studies such as [52], [53], [54], [55], and [56]. In this work, the key hyperparameters of this sequence of operations involving Takens' embedding, complex construction, persistent homology, and persistent landscape are set as follows:

- Takens' Embedding Theorem: The time delay is set to  $\tau = 1$ , and the reconstructed dimension is set to  $m = 3$ .
- Vietoris-Rips Complex: The homology dimensions are set to  $[0, 1, 2]$ , and a 2-module is employed.
- Persistent Landscape: The number of layers is set to 1, and  $T$  is set to 100.

Therefore, for  $x_i \in \mathbb{R}$ , we have  $\mathbf{F} \in \mathbb{R}^{1 \times 12}$  (Equation 23). For  $x_i \in \mathbb{R}^d$ , we repeat the above process for all features in the time series and obtain a matrix  $\mathbf{F} \in \mathbb{R}^{d \times 12}$ . For mini-batch samples, the topological feature matrix becomes  $\mathbf{F} \in \mathbb{R}^{B \times d \times 12}$ .  $\mathbf{F}$  was then passed through a Tanh activation function to normalize to  $[-1, 1]$ .

### 2.3 Generative Adversarial Network

Generative Adversarial Networks (GANs) [57] introduce a framework that transforms a unsupervised task to a supervised one. One model,  $G$  (Generator), is tasked with synthesizing data samples that resemble those drawn from an unknown data distribution. The other model,  $D$  (Discriminator), classifies real data from those generated by  $G$ . Given noise  $z$  from the distribution  $p_z(z)$

$$G(z; \theta_G) \mapsto x_{\text{fake}}. \quad (24)$$

Simultaneously, the discriminator receives input  $x$  and predicts the probability that it originates from the true data distribution:

$$D(x; \theta_D) \in [0, 1]. \quad (25)$$

Training a GAN involves solving a two-player minimax optimization problem. The value function governing this interaction is defined as:

$$\min_G \max_D V(D, G) = \mathbb{E}_{x \sim p_{\text{data}}(x)} [\log D(x)] + \mathbb{E}_{z \sim p_z(z)} [\log(1 - D(G(z)))] \quad (26)$$

From the discriminator's perspective, the goal is to maximize its ability to make accurate classifications:

$$\max_D \mathbb{E}_{x \sim p_{\text{data}}(x)} [\log D(x)] + \mathbb{E}_{z \sim p_z(z)} [\log(1 - D(G(z)))] \quad (27)$$

Conversely, the generator attempts to produce outputs that the discriminator cannot reject, effectively minimizing the second term:

$$\min_G \mathbb{E}_{z \sim p_z(z)} [\log(1 - D(G(z)))] \quad (28)$$

Through this adversarial interplay, both models iteratively improve until the generator produces outputs that are statistically indistinguishable.

### 3 Problem Formulation

Given a time-series  $X_{1:L} = \{x_1, x_2, \dots, x_L\}$  from the observed data space  $\mathcal{X} \subseteq \mathbb{R}^{L \times d}$  and the topological feature space  $\mathcal{T} \subseteq \mathbb{R}^{d \times d}$  that corresponds to the time-series, this work aims to solve three problems:

1. Persistent homology extracts topological features from time-series data through a deterministic mapping:

$$f : \mathcal{X} \rightarrow \mathcal{T}, \quad (29)$$

where  $f$  is a sequence of operations involving Takens Embedding, complex construction, persistent homology, and persistent landscape. However, this process is computationally slow, as will be discussed in the subsequent section. The high computational cost is inevitable in both the training and inference phases. To address this limitation, we aim to develop a parameterized network  $\text{Net}_\theta$  that learns the function  $f$  by treating topological features as latent variables. Specifically, the network is designed to approximate the mapping:

$$\text{Net}_\theta : \mathcal{X} \rightarrow \mathcal{T}, \quad (30)$$

or alternatively, to learn the probabilistic relationship:

$$\text{Net}_\theta : \mathbb{P}_\theta(\mathcal{T} | \mathcal{X}), \quad (31)$$

under the supervision of  $f$  during the training phase. Although this approach may increase computational time during training, it significantly accelerates the extraction of topological features during inference.

2. We aimed to obtain flexible topological representations. The mapping  $f$  does not provide any intermediate representations of topological features between the observed data space and the topological feature space. This end-to-end mapping may lead to overly specific representations, limiting the flexibility and generalizability of the extracted features. To address this, we introduce a latent space  $\mathcal{Z}$ , which serves as the hidden layer outputs of the neural network  $\text{Net}_\theta$ . Specifically, we redefine the mapping as follows:

$$\text{Net}_\theta : \mathcal{X} \xrightarrow{h_1} \mathcal{Z}_1 \xrightarrow{h_2} \dots \xrightarrow{h_{n-1}} \mathcal{Z}_{n-1} \xrightarrow{h_n} \mathcal{T}, \quad (32)$$

where  $h_i$  indicates the hidden layer of  $\text{Net}_\theta$ . In other words, these mappings can be viewed as normalizing flows [58], which transform data into the complex space of topological features through a sequence of transformation functions.

3. To integrate the pre-trained topological feature extractor  $\text{Net}_\theta$  into a real application, we propose an enhanced forecasting approach. Given a time-series, instead of predicting the future using:

$$\mathbb{P}_{\hat{\theta}}(\mathbf{x}_{L+1:L+t} \mid x_1, \dots, x_L), \quad (33)$$

where  $\hat{\theta}$  is learned through a prediction loss:

$$\text{pred\_loss}(\hat{\mathbf{x}}_{L+1:L+t}, \mathbf{x}_{L+1:L+t}), \quad (34)$$

and  $\hat{\mathbf{x}}_{L+1:L+t}$  is the prediction of  $\mathbf{x}_{L+1:L+t}$ , we enhance forecast accuracy by incorporating topological features. Specifically, we predict the future as follows:

$$\mathbb{P}_{\hat{\theta}}(\mathbf{x}_{L+1:L+t} \mid x_1, \dots, x_L, \text{Net}_\theta(x_1, \dots, x_L)), \quad (35)$$

where  $\hat{\theta}$  is learned through a combined loss function:

$$\begin{aligned} & \text{pred\_loss}(\hat{\mathbf{x}}_{L+1:L+t}, \mathbf{x}_{L+1:L+t}) + \\ & \text{topo\_loss}(\text{Net}_\theta(\hat{\mathbf{x}}_{L+1:L+t}), \text{Net}_\theta(\mathbf{x}_{L+1:L+t})) + \\ & \text{topo\_loss}(h_\theta(\hat{\mathbf{x}}_{L+1:L+t}), h_\theta(\mathbf{x}_{L+1:L+t})), \end{aligned} \quad (36)$$

where the topological reconstruction loss  $\text{topo\_loss}$  encourages the predicted time-series to preserve the underlying topological structure of the ground truth time-series, and  $h_\theta$  indicates representations from the hidden layers of  $\text{Net}_\theta$ . Unlike previous approaches that utilize topological features extracted from a deterministic process, we extract these features from a pre-trained network and incorporate them directly into the training loss.

## 4 Proposed Methods

### 4.1 Topological Feature Extractors

A straightforward approach to train  $\text{Net}_\theta$  under the supervision of the topological mapping  $f$  is to learn the parameter set  $\theta$  by minimizing a loss function that measures the discrepancy between the synthetic topological features generated by  $\text{Net}_\theta$  and the real topological features, as shown in the top part of Figure 1. In the figure, Configuration 0 refers to the chain of operations involving Takens' Embedding Method (TEM), complex construction, persistent homology (PH), and persistent landscape (PL), as discussed in Section 2.2.3 and shown in Figure 2.

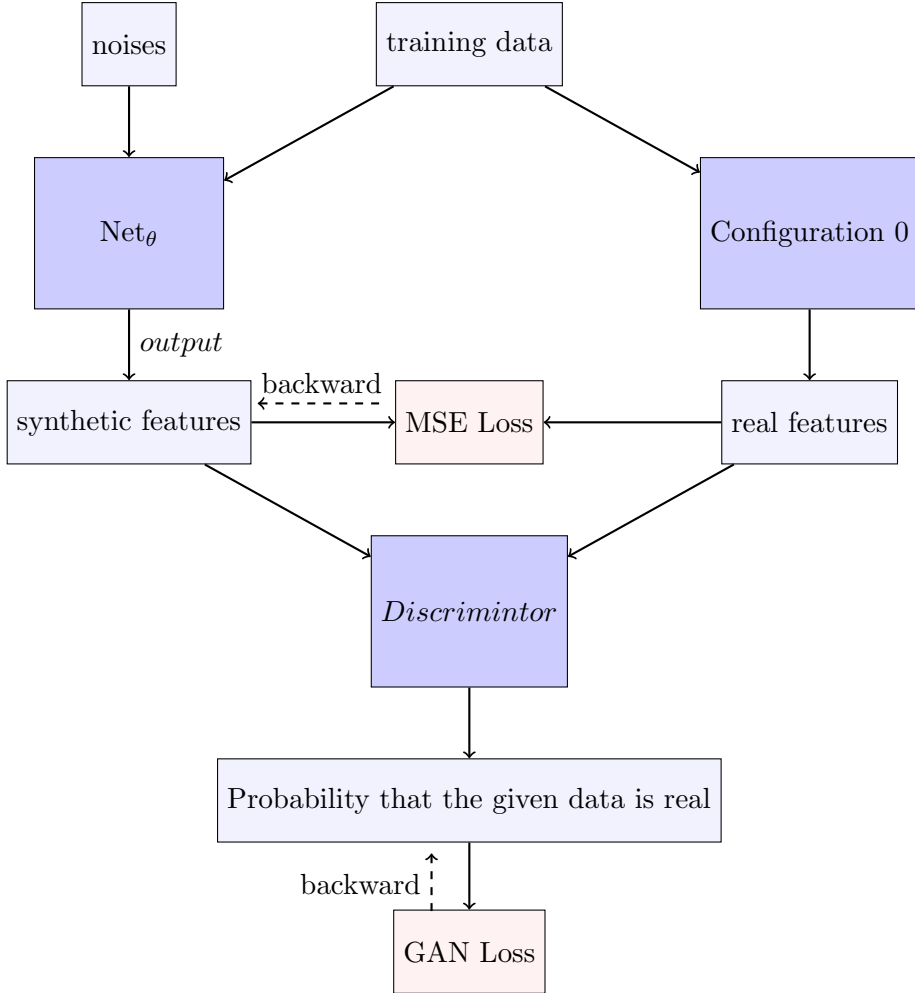


Figure 1: The working flow of training  $\text{Net}_\theta$ .

However, in the experiment, we observed that although the synthetic topological features generated by  $\text{Net}_\theta$  were close to the real topological features, they followed different distributions (details are provided in Section 6.3). To bridge this gap, we leveraged the GAN structure, which allows the generator to learn the statistical characteristics of the target distribution. Consequently, we developed  $\text{Net}_\theta$  within a GAN framework to better capture the underlying distribution of the real topological features. The complete workflow is illustrated in Figure 1. Training data is processed through Configuration 0 to produce real topological features using Takens' embedding, Vietoris-Rips complex, persistent homology, and persistent landscape. The synthetic and real topological features are compared using MSE Loss, and the discriminator forces  $\text{Net}_\theta$  to learn the underlying distribution of the topological features by GAN Loss. This hybrid learning strategy leverages both MSE Loss for accuracy and GAN Loss for distribution alignment, enabling  $\text{Net}_\theta$  to effectively learn the complex distribution of real topological features. GAN Loss can be implemented as vanilla loss [57], Wasserstein loss with gradient penalty [59], or least squares loss [60]. In this study, we experimented with all three variants and found that vanilla loss provided more stable training and better convergence.

Suppose  $\mathcal{T}$  denotes the real topological features and  $\hat{\mathcal{T}}$  represents the synthetic features generated by  $\text{Net}_\theta$ . We train  $\text{Net}_\theta$  by minimizing the following loss function:

$$\text{Loss} = \text{GAN\_Loss} + \lambda \cdot \text{Topo\_Loss}, \quad (37)$$

where

$$\text{GAN\_Loss} = -\mathbb{E}_{\mathbb{P}(\hat{\mathcal{T}}|\mathcal{X}, Z)}[\log D(\text{Net}_\theta(X, Z))] \quad (38)$$

and

$$\text{Topo\_Loss} = \mathbb{E}_{\mathbb{P}(\hat{\mathcal{T}}|\mathcal{X}, Z)} \|\mathcal{T} - \hat{\mathcal{T}}\|_2^2 \quad (39)$$

We set  $\lambda = 1.0$  in this work. Depending on the specific implementations of  $\text{Net}_\theta$  and  $G$ , we experimented with three different configurations, ranging from simple to complex, as detailed in the following sections.

### Configuration 1

In the first configuration, both  $\text{Net}_\theta$  and  $G$  are implemented using three layers of Gated Recurrent Units (GRU), followed by a dense layer and an activation function. Specifically,  $\text{Net}_\theta$  utilizes a Tanh activation function after the dense layer, while  $G$  employs a Sigmoid activation function. The detailed architecture is illustrated in Figure 3.

The reason of employing GRU is that recurrent neural networks (GRU) have been effectively utilized in synthesizing time-series data and learning latent variables in models such as CRNNGAN [61], RCGAN [62], and TimeGAN [63]. In our experiments, we explored different architectures, including RNN, LSTM, and GRU. Among these, GRU demonstrated the most stable GAN loss and reconstruction loss for topological features during training.

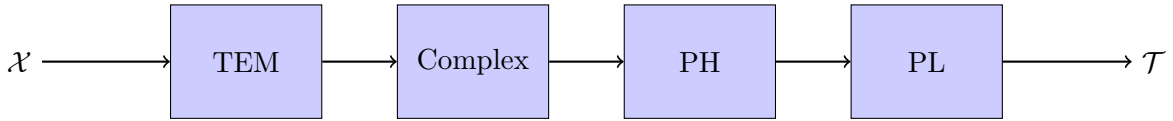


Figure 2: The working flow of Configuration 0.

### Configuration 2

In Configuration 2, we introduced a reconstructor  $R_\theta$  to map the topological latent space back to the observed data space:

$$\text{Net}_\theta : \mathcal{X} \rightarrow \mathbb{P}(\mathcal{T}|\mathcal{X}), \quad R_\theta : \mathbb{P}(\mathcal{T}|\mathcal{X}) \rightarrow \mathbb{P}(\mathcal{X}|\mathcal{T}). \quad (40)$$

Before training  $\text{Net}_\theta$  and  $G$ , we pre-train  $\text{Net}_\theta$  and  $R_\theta$ , as illustrated in Figure 4. During the training,  $\theta$  is updated by:

$$\mathbb{E}_{\mathbb{P}(\hat{\mathcal{X}}|\hat{\mathcal{T}})} \|\mathcal{X} - \hat{\mathcal{X}}\|_2^2, \quad (41)$$

where  $\hat{\mathcal{X}}$  denotes the reconstructed data by  $R_\theta$ . This approach ensures that the parameters of  $\text{Net}_\theta$  start from a more optimal initial point, leading to improved model performance and more accurate reconstruction of the observed data space. The implementation of  $\text{Net}_\theta$  and  $G$  follows the structure used in Configuration 1, and the RNN layers are configured as GRU networks.  $R_\theta$  is designed as a mirrored version of  $\text{Net}_\theta$ , beginning with a dense layer followed by three layers of GRU.

### Configuration 3

In Configuration 3, we introduced a stacked-CGAN structure. In addition to  $\text{Net}_\theta$  and  $R_\theta$  that distinguishes synthetic features from true features, we incorporated an additional discriminator  $D_\theta^\mathcal{X}$ . This discriminator distinguishes between true data and synthetic data  $\mathcal{X}$  generated by  $R_\theta$ . Before training  $\text{Net}_\theta$  and  $D_\theta^\mathcal{X}$ , we first trained  $\text{Net}_\theta$  and  $R_\theta$ , and  $D_\theta^\mathcal{X}$  by minimizing the following objective:

$$\mathbb{E}_{\mathbb{P}(\hat{\mathcal{X}}|\hat{\mathcal{T}})} \left[ \|\mathcal{X} - \hat{\mathcal{X}}\|_2^2 \right] - \mathbb{E}_{\mathbb{P}(\hat{\mathcal{X}}|\hat{\mathcal{T}})} \left[ \log D_\theta^\mathcal{X}(R_\theta(\hat{\mathcal{T}})) \right], \quad (42)$$

and  $D_\theta^{\mathcal{X}}$  by

$$-\mathbb{E}_{\mathbb{P}(\mathcal{X})} [\log D_\theta^{\mathcal{X}}(\mathcal{X})] - \mathbb{E}_{\mathbb{P}(\hat{\mathcal{X}}|\hat{\mathcal{T}})} [1 - \log D_\theta^{\mathcal{X}}(R_\theta(\hat{\mathcal{T}}))]. \quad (43)$$

The network architecture was implemented using a 3-layer GRU. The workflow of this configuration is illustrated in Figure 5. The training process consisted of two phases:

1. First Phase: Involving the pipeline  $\text{Net}_\theta \rightarrow R_\theta \rightarrow D_\theta^{\mathcal{X}}$ .
2. Second Phase: Involving the pipeline  $\text{Net}_\theta \rightarrow D_\theta^{\mathcal{T}}$ .

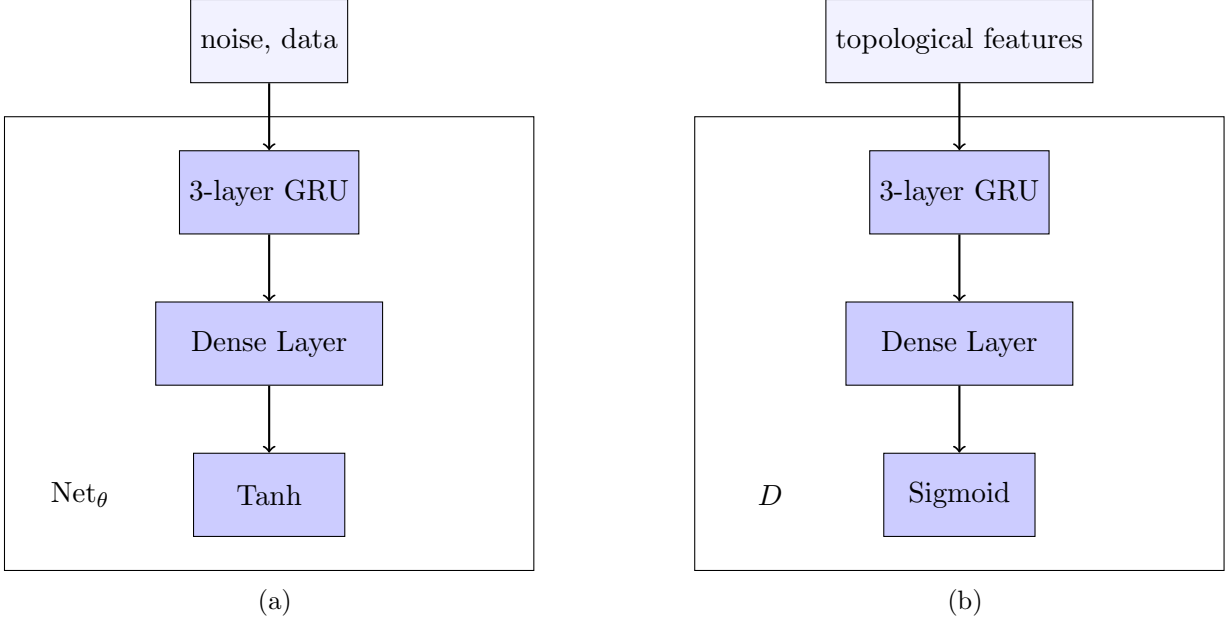


Figure 3: The architectures of  $\text{Net}_\theta$  (a) and  $G$  (b) for Configuration 1.

## Training

Suppose the data is  $\mathbf{X} \in \mathbb{R}^{N \times d}$ , where  $N$  is the total number of samples and  $d$  is the data dimension,  $E$  is the total number of training epochs, and  $L$  is the sequence length. The following training strategies are adopted:

1. We utilized Adam optimizers with a fixed learning rate of  $\text{lr} = 1 \times 10^{-3}$  and betas set to  $(0.9, 0.999)$ , without applying any learning rate decay strategy. In Configuration 2, the learning rate of the optimizer for  $R_\theta$  was set to  $1 \times 10^{-3}$  when  $L < 168$ , and to  $2 \times 10^{-3}$  when  $L \geq 168$ . In Configuration 3, the learning rate for  $R_\theta$  was set to  $1 \times 10^{-3}$  when  $L < 96$ , and to  $2 \times 10^{-3}$  when  $L \geq 96$ .
2. The batch size  $B$  is set to 128. At each training epoch, the rows of  $\mathbf{X}$  are permuted, and an integer is randomly selected from the range  $[0, N - L - 1]$ . This process is repeated  $B$  times to generate sequences of length  $L$ , forming the training batch  $X \in \mathbb{R}^{B \times L \times d}$ . Noises of the same size as  $X$  are sampled from the normal distribution  $Z \sim \mathcal{N}(0, 1)$ .
3. For RNNs, the hidden size is set to be four times the input size. Specifically, for  $\text{Net}_\theta$ , the hidden size in its RNN layers is configured as  $4(d + \dot{d})$ , where  $d$  represents the dimension of the input data and  $\dot{d}$  denotes the dimension of the topological features.
4. During training, we dynamically adjusted the number of updates  $k$  for the parameters of  $\text{Net}_\theta$  based on the ratio of average Generator and Discriminator losses:

- $k$  was increased by 1 if  $\frac{\mathbb{E}[\mathcal{L}_{\text{Net}_\theta}]}{\mathbb{E}[\mathcal{L}_D]} > 0.7$ , and the maximum is 10.
- $k$  was decreased by 1 if  $\frac{\mathbb{E}[\mathcal{L}_{\text{Net}_\theta}]}{\mathbb{E}[\mathcal{L}_D]} \leq 0.7$ , and the minimum is 1.

Here,  $\mathbb{E}[\mathcal{L}_{\text{Net}_\theta}]$  and  $\mathbb{E}[\mathcal{L}_D]$  denote the Generator and Discriminator losses averaged over all completed training epochs up to the current epoch, respectively.

5. The number of training epochs  $E$  is set according to the sequence length  $L$ . In this study,  $L$  varies within the set  $\{6, 12, 24, 36, 48, 96, 168, 336\}$ , and the early stopping is adopted and triggered when  $\text{Topo\_Loss}_{E+1} > \text{Topo\_Loss}_E + 0.1$ .
6. The dropout rate is set to 0.0 after testing values from the set  $\{0.0, 0.2, 0.4, 0.5\}$ , where 0.0 resulted in the most stable training and the lowest reconstruction loss. The RNNs are configured to be unidirectional, as using bidirectional RNNs showed no significant improvement in performance.

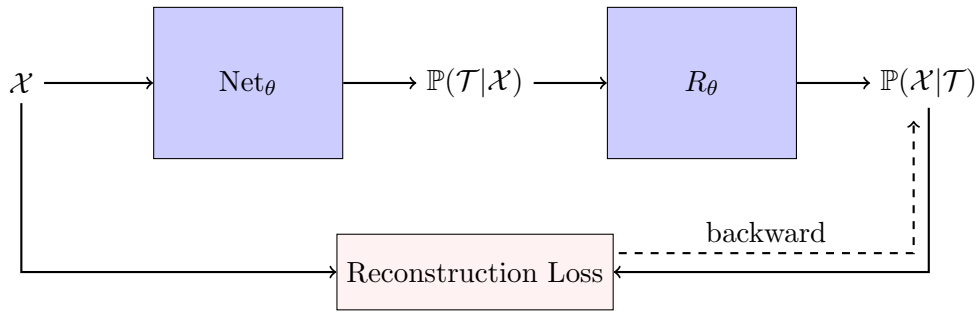


Figure 4: The working flow of  $\text{Net}_\theta$  and  $R_\theta$  for Configuration 2.

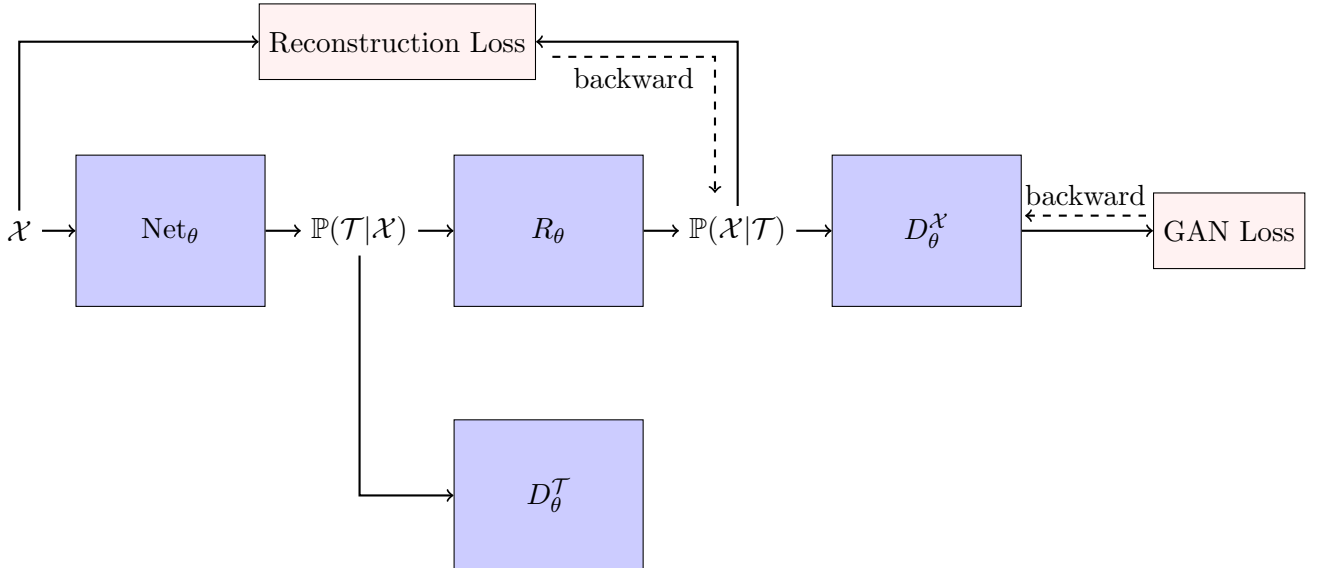


Figure 5: The working flow of Configuration 3.

## 4.2 Topological Information Supervised Predictor

To enhance the accuracy of time-series forecasting, we propose a novel architecture that leverages topological features extracted from a pre-trained neural network,  $\text{Net}_\theta$ . Traditional forecasting

methods often focus solely on temporal dependencies, neglecting the underlying topological structures that can provide valuable insights into the data's geometric and dynamic properties.

The Figure 6(a) presents the training phase of an advanced forecasting architecture that integrates topological features extracted from a pre-trained neural network,  $\text{Net}_\theta$ , to enhance the accuracy of time-series predictions. This approach differs from traditional forecasting methods by explicitly preserving the topological structure of the data throughout the prediction process. The model takes two primary inputs:

1.  $X_{1:L}$ : Historical time-series data of length  $L$ .
2.  $Y_{L+1:L+t}$ : Future observations of length  $t$  used for training and evaluation.
3.  $\mathcal{T}_{X_{1:L}}$ : Topological features from the historical data.
4.  $\mathcal{T}_{Y_{L+1:L+t}}$ : Topological features from the future observations.
5.  $\mathcal{Z}_{Y_{L+1:L+t}}$ : Latent representations from the hidden layers of  $\text{Net}_\theta$ , capturing complex temporal dependencies.

The extracted topological features  $\mathcal{T}_{X_{1:L}}$  are fed into the Topological Embedder  $TE_{\hat{\theta}}$ , which maps these features into an embedding space suitable for forecasting. The resulting embedded features are then concatenated with the original historical data  $X_{1:L}$ , forming an enriched representation that combines temporal patterns and topological structures. This combined representation is subsequently input to the Predictor  $P_{\hat{\theta}}$ .

$P_{\hat{\theta}}$  generates the forecast  $\hat{Y}_{L+1:L+t}$ , which aims to approximate the true future values  $Y_{L+1:L+t}$ . The prediction pathway is designed to maintain the temporal dependencies captured by the historical data while leveraging the additional topological context. The model is trained using a combined loss function consisting of a prediction loss

$$\text{pred\_loss} \left( \hat{Y}_{L+1:L+t}, Y_{L+1:L+t} \right) \quad (44)$$

which measures the discrepancy between the predicted future values and the true observations, and a topological loss that is consisted of topological feature consistency loss

$$\text{topo\_loss} \left( \text{Net}_\theta(\hat{Y}_{L+1:L+t}), \text{Net}_\theta(Y_{L+1:L+t}) \right) \quad (45)$$

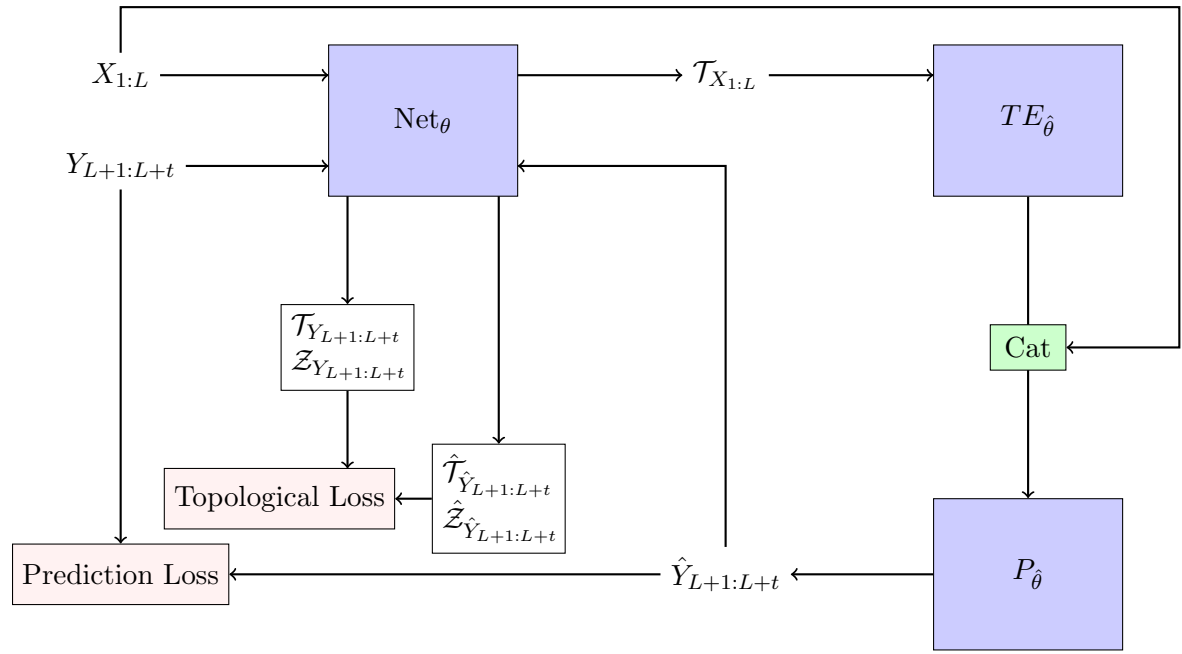
and latent space consistency loss:

$$\text{topo\_loss} \left( \mathcal{Z}_\theta(\hat{Y}_{L+1:L+t}), \mathcal{Z}_\theta(Y_{L+1:L+t}) \right) \quad (46)$$

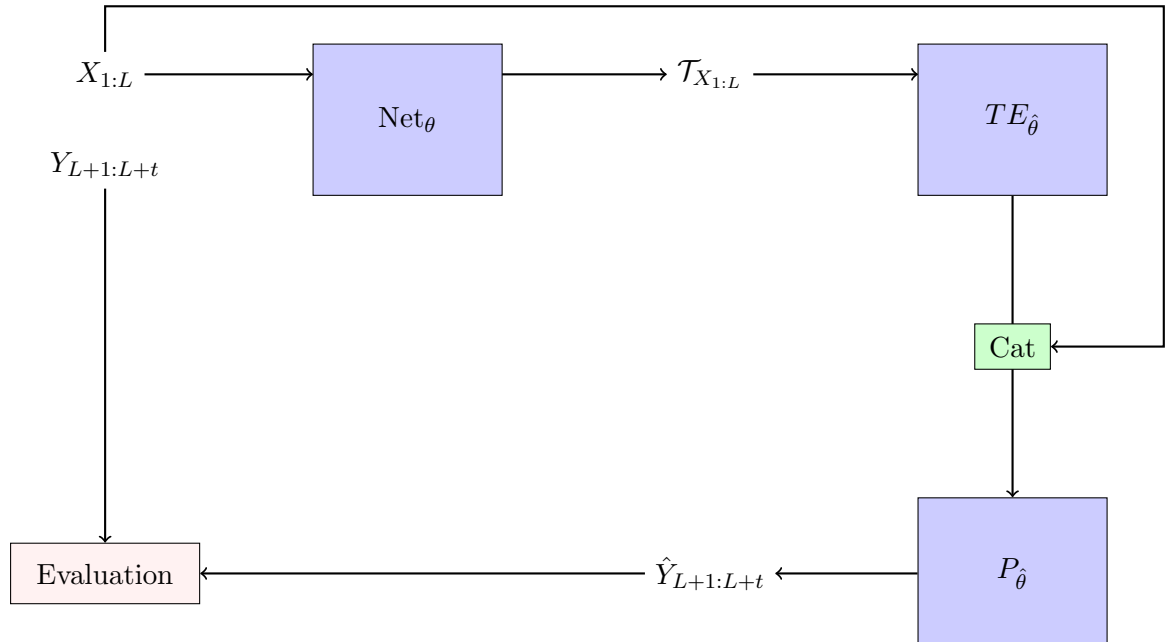
The topological feature consistency loss compares the topological features extracted from the predicted and true sequences, enforcing consistency in the high-level topological patterns. The latent space consistency loss compares the latent representations  $\mathcal{Z}$  from the hidden layers of  $\text{Net}_\theta$ , ensuring that the internal dynamics of the predicted and true sequences remain topologically consistent. The total loss is:

$$\text{pred\_loss} + \lambda \cdot \text{topo\_loss}. \quad (47)$$

The Figure 6(b) presents the inference phase. Unlike the training phase, the inference phase does not include any loss computation. During inference, the model simply generates predictions without any gradient updates. The historical input  $X_{1:L}$  is passed through  $\text{Net}_\theta$  to extract topological features  $\mathcal{T}_{X_{1:L}}$ , which are then embedded and concatenated with the original input. This combined feature set is fed into the predictor  $P_{\hat{\theta}}$  to produce  $\hat{Y}_{L+1:L+t}$ . Predictions are generated as  $\hat{Y}_{L+1:L+t}$  and are directly evaluated, which compares them to the ground truth  $Y_{L+1:L+t}$  using predefined metrics.



(a) Traing Phase



(b) Inference Phase

Figure 6: Training phase (a) and Inference phase (b) for TIS-predictor.

## 5 Experiments

### 5.1 Dataset

This study utilizes three distinct datasets to evaluate the effectiveness of pre-trained topological feature extractors in enhancing forecasting accuracy. These datasets offer comprehensive insights into electric power deployment, oceanographic dynamics, and air quality monitoring. Each dataset is carefully chosen to capture unique temporal and spatial characteristics relevant to its domain, providing a robust foundation for analyzing forecasting performance. The datasets are detailed as follows:

- Electricity Transformer Temperature <sup>1</sup>: The ETT is a crucial indicator for long-term electric power deployment. It contains 2 years of data from two separate counties in China. It was divided into two distinct datasets: **ETTh1** and **ETTh2**, both at the 1-hour level. Each dataset contains two years of data (2 year  $\times$  365 days  $\times$  24 hours). Details of the data variables are provided in Table 1.
- Ocean Meteorological and Temperature Data <sup>2</sup>: We collected data on nine variables related to oceanographic, weather, and atmospheric conditions from two monitoring stations, **C46207** and **C46208**, located along the Pacific Northwest Coast of Canada. This region is critical for monitoring oceanographic dynamics influenced by the Pacific Ocean, including wave patterns, sea surface temperatures, and ocean circulation. The dataset covers the period from January 1, 2010, to December 31, 2018 (9 year  $\times$  365 days  $\times$  24 hours). Detailed information about the collected data is provided in Table 2.
- Air Pollution Data: Hourly average pollution concentration data was obtained from the Department of Environment (DOE) [64], Malaysia for the period 2018-2019 (2 year  $\times$  365 days  $\times$  24 hours). The dataset includes 13 atmospheric and environmental variables. It consists of two separate datasets collected from the air monitoring stations **CA06P** and **CA09P**, both located on Penang Island, an island known for its strategic location along the Strait of Malacca, making it a key urban and industrial hub in Malaysia. Details of the data variables are provided in Table 3.

For each dataset, we divided 70% for training and 30% for testing. For each sample  $X = (x_1, \dots, x_d)$ , where  $d$  is the dimension of the data, we normalized it by:

$$X' = \frac{X - \min(X_{\text{train}})}{\max(X_{\text{train}}) - \min(X_{\text{train}}) + \epsilon}, \quad (48)$$

where  $X'$  is the normalized data sample,  $X_{\text{train}}$  refers to the training set,  $\min(X_{\text{train}})$  and  $\max(X_{\text{train}})$  are of shape  $1 \times d$  and denote the minimum and maximum values of the training set, respectively. The small constant  $\epsilon$  is set to  $1 \times 10^{-8}$  and added for numerical stability, preventing division by zero. The training data is used to train the topological feature extractors and predictors, while the testing data is reserved for evaluation.

We conducted all of our experiments, including those in the Ablation Study, on a computing device equipped with two NVIDIA RTX 4090D GPUs, each with 24 GB of GDDR6X memory, powered by an Intel Xeon Platinum 8474C processor, and with 80 GB of RAM. The system operates on Ubuntu 22.04 with Python 3.12 and PyTorch 2.5.1, leveraging CUDA 12.4 for efficient GPU acceleration. For model development, we primarily utilized the libraries PyTorch, Scikit-learn, Giotto-TDA, and SciPy.

<sup>1</sup>Data Link: <https://github.com/zhouhaoyi/ETDataset>

<sup>2</sup>Data Link: <https://meds-sdmm.dfo-mpo.gc.ca/isdm-gdsi/index-eng.html>

Table 1: Description of Features in the ETT Dataset

Field	Description	Unit
HUFL	High UseFul Load	MW (Megawatts)
HULL	High UseLess Load	MW (Megawatts)
MUFL	Middle UseFul Load	MW (Megawatts)
MULL	Middle UseLess Load	MW (Megawatts)
LUFL	Low UseFul Load	MW (Megawatts)
LULL	Low UseLess Load	MW (Megawatts)
OT	Oil Temperature (target)	°C (Celsius)

Table 2: Wave and Weather Parameters

Parameter	Description	Units
VCAR	Characteristic significant wave height (calculated by MEDS)	m
VTPK	Wave spectrum peak period (calculated by MEDS)	s
VCMX	Maximum zero crossing wave height (reported by the buoy)	m
WDIR	Direction from which the wind is blowing	° True
WSPD	Horizontal wind speed	m/s
GSPD	Gust wind speed	m/s
ATMS	Atmospheric pressure at sea level	mbar
DRYT	Dry bulb temperature	°C
SSTP	Sea surface temperature	°C

Table 3: Description of Air Pollution Data Variables

Variable	Description	Unit
PM <sub>10</sub>	Particulate Matter (diameter $\leq 10 \mu\text{m}$ )	µg/m <sup>3</sup>
PM <sub>2.5</sub>	Particulate Matter (diameter $\leq 2.5 \mu\text{m}$ )	µg/m <sup>3</sup>
SO <sub>2</sub>	Sulfur Dioxide	ppm
NO <sub>2</sub>	Nitrogen Dioxide	ppm
NO	Nitric Oxide	ppm
NOX	Nitrogen Oxides (NO + NO <sub>2</sub> )	ppm
O <sub>3</sub>	Ozone	ppm
CO	Carbon Monoxide	ppm
WD	Wind Direction	°
WS	Wind Speed	m/s
RH	Relative Humidity	%
SR	Solar Radiation	W/m <sup>2</sup>
AT	Ambient Temperature	°C

## 5.2 Short-term prediction

For short-term prediction, we developed a straightforward model consisting of a 2-layer GRU followed by a dense layer with a Sigmoid activation function (shown in Figure 7(a)). In the total loss function (Equation 47), we set the hyperparameter  $\lambda = 5.0$ , ensuring that the topological

loss is on a comparable scale with the prediction loss. The topological loss and prediction loss are both implemented as  $L_2$  loss. The prediction length  $t$  was chosen from the set  $\{6, 12, 24, 36\}$ .

Since short-term prediction is relatively simpler compared to long-term forecasting, no contextual information was provided to the predictor. Specifically, if  $y$  is the target variable, its historical data was excluded from the input variables  $X$  fed to the predictor. We also employed unrolled training and testing. In this approach, given the input sequence  $\mathbf{x}_{1:L}$ , the model predicts the next sequence  $\mathbf{y}_{L+1:L+t}$ . The input window then shifts forward, using  $\mathbf{x}_{L:2L}$  to predict  $\mathbf{y}_{L+t+1:L+2t}$ , and so on. We set the prediction length equal to the sequence length of input variables, in other words,  $L = t$ .

The training configuration was set with 3000 epochs, a batch size of 128, and a learning rate of  $1 \times 10^{-3}$  using the Adam optimizer. During each epoch, a batch of samples was randomly selected for training, following the workflow illustrated in Figure 6(a). The hidden sizes of BiGRU layers were set as four times of the dimension of the input variables. Dropout rate was set to 0.0. We also introduced a topological embedder, as shown in Figure 7(b), is composed of a sequence of fully connected layers with SiLU (Sigmoid Linear Unit [65]) activation functions, defined as

$$\text{SiLU}(x) = x \cdot \text{sigmoid}(x). \quad (49)$$

It is designed to transform topological features into a representation suitable for time-series prediction. The embedder outputs the engineered topological features with dimensions matching those of the input data. This structure draws inspiration from the use of dense layers with activation functions in diffusion models [66, 67, 68], which effectively capture time embedding, token embedding, and position embedding.

To ensure robustness and reliability, the training and inference process was repeated 10 times for each dataset. Afterward, the Mean Square Error (MSE), Mean Absolute Error (MAE), and Root Mean Square Error (RMSE) were calculated along with their standard deviations across the 10 runs, providing a comprehensive evaluation of model performance and variability.

For the electric datasets ETTh1 and ETTh2, Oil Temperature (OT) was chosen as the target variable, since OT is crucial for monitoring and maintaining the performance of electricity transformers. For the oceanography datasets C46207 and C46208, Characteristic Significant Wave Height (VCAR) and Maximum Zero Crossing Wave Height (VCMX) were selected as the target variables, since they are critical parameters for understanding ocean wave dynamics and often used in marine engineering and navigation safety. For the air pollution datasets CA06P and CA09P, PM<sub>10</sub> and PM<sub>2.5</sub> were chosen as the target variables. These pollutants are significant indicators of air quality and have substantial health implications. The remaining variables were used as input features to capture the contextual information influencing the target variables. These choices were made based on the importance and relevance of each variable in its respective domain, as detailed in Tables 1 to 3.

Tables 4, 5, and 6 present the evaluation results for six datasets using the metrics of MSE, MAE, and RMSE

$$\text{MSE} = \frac{1}{N} \sum_{i=1}^N (y_i - \hat{y}_i)^2, \quad \text{MAE} = \frac{1}{N} \sum_{i=1}^N |y_i - \hat{y}_i|, \quad \text{RMSE} = \sqrt{\frac{1}{N} \sum_{i=1}^N (y_i - \hat{y}_i)^2}, \quad (50)$$

respectively, where  $y_i$  is the ground true and  $\hat{y}_i$  is the prediction. The results are displayed in the format of "mean  $\pm$  standard deviation," where the mean value is calculated across 10 runs, and the standard deviation represents the variability of the performance across these runs. In the table headers, "Data" refers to the type of dataset used in the experiments. Labels such as "Cfg 1" or similar formats correspond to the predictors where topological features are incorporated into both the training and inference phases, as proposed in Section 4.2.

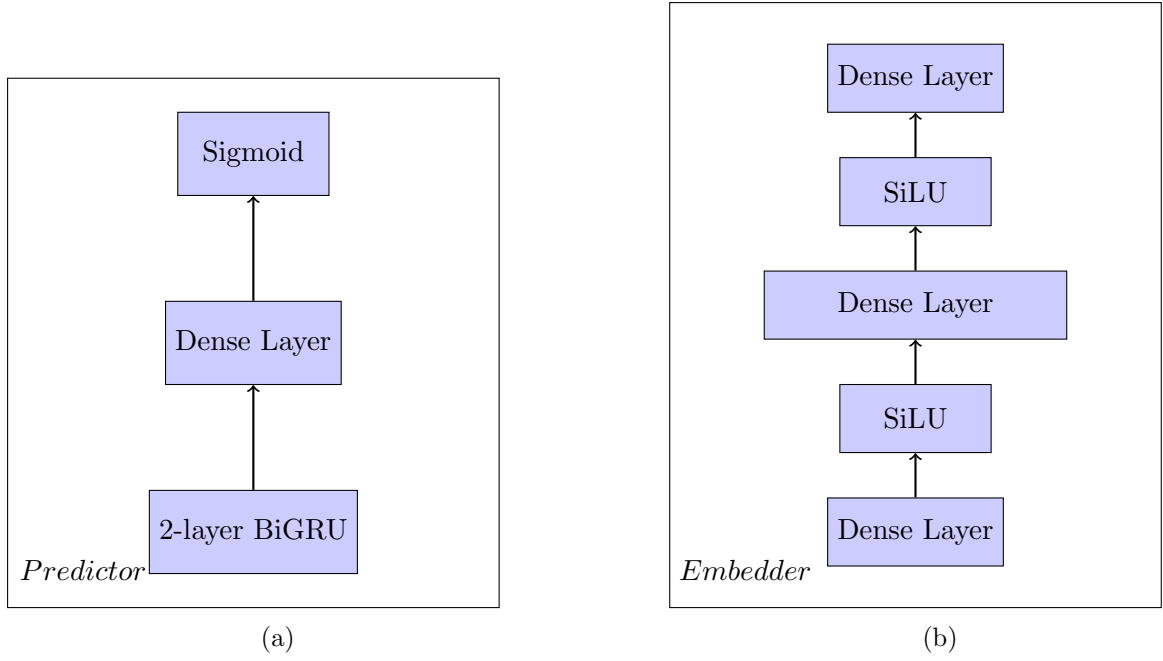


Figure 7: The architectures of Predictor (a) and Topological Embedder (b).

Table 4: MSE of short-term predictions.

Data	Step	BiGRU	Cfg 1	Cfg 2	Cfg 3
ETTh1	6-hour	$0.0511 \pm 0.0102$	$0.0024 \pm 0.0004$	$0.0021 \pm 0.0002$	<b><math>0.0012 \pm 0.0002</math></b>
	12-hour	$0.0320 \pm 0.0108$	$0.0029 \pm 0.0007$	$0.0020 \pm 0.0003$	<b><math>0.0019 \pm 0.0002</math></b>
	24-hour	$0.0185 \pm 0.0053$	$0.0044 \pm 0.0013$	$0.0023 \pm 0.0002$	<b><math>0.0021 \pm 0.0002</math></b>
	36-hour	$0.0235 \pm 0.0072$	$0.0052 \pm 0.0023$	$0.0027 \pm 0.0002$	<b><math>0.0026 \pm 0.0003</math></b>
ETTh2	6-hour	$0.0311 \pm 0.0043$	$0.0148 \pm 0.0030$	$0.0098 \pm 0.0002$	<b><math>0.0096 \pm 0.0002</math></b>
	12-hour	$0.0248 \pm 0.0036$	$0.0151 \pm 0.0020$	$0.0157 \pm 0.0012$	<b><math>0.0151 \pm 0.0014</math></b>
	24-hour	$0.0300 \pm 0.0052$	$0.0108 \pm 0.0026$	<b><math>0.0063 \pm 0.0004</math></b>	$0.0065 \pm 0.0005$
	36-hour	$0.0367 \pm 0.0044$	$0.0133 \pm 0.0024$	$0.0140 \pm 0.0011$	<b><math>0.0116 \pm 0.0010</math></b>
C46207	6-hour	$0.0037 \pm 0.0003$	<b><math>0.0016 \pm 0.0002</math></b>	$0.0018 \pm 0.0002$	$0.0017 \pm 0.0003$
	12-hour	$0.0038 \pm 0.0003$	<b><math>0.0018 \pm 0.0003</math></b>	$0.0021 \pm 0.0003$	$0.0019 \pm 0.0003$
	24-hour	$0.0048 \pm 0.0002$	$0.0027 \pm 0.0003$	$0.0033 \pm 0.0002$	<b><math>0.0025 \pm 0.0002</math></b>
	36-hour	$0.0055 \pm 0.0002$	<b><math>0.0030 \pm 0.0003</math></b>	$0.0042 \pm 0.0002$	$0.0032 \pm 0.0003$
C46208	6-hour	$0.0072 \pm 0.0054$	$0.0059 \pm 0.0022$	$0.0061 \pm 0.0023$	<b><math>0.0048 \pm 0.0021</math></b>
	12-hour	$0.0085 \pm 0.0091$	$0.0092 \pm 0.0037$	$0.0075 \pm 0.0030$	<b><math>0.0071 \pm 0.0039</math></b>
	24-hour	$0.0056 \pm 0.0038$	<b><math>0.0036 \pm 0.0012</math></b>	$0.0044 \pm 0.0016$	$0.0042 \pm 0.0019$
	36-hour	$0.0070 \pm 0.0032$	<b><math>0.0060 \pm 0.0029</math></b>	$0.0064 \pm 0.0025$	$0.0068 \pm 0.0022$
CA06P	6-hour	$0.0051 \pm 0.0003$	$0.0047 \pm 0.0003$	<b><math>0.0045 \pm 0.0002</math></b>	$0.0048 \pm 0.0002$
	12-hour	$0.0054 \pm 0.0002$	<b><math>0.0049 \pm 0.0002</math></b>	$0.0052 \pm 0.0003$	$0.0051 \pm 0.0002$
	24-hour	$0.0072 \pm 0.0006$	$0.0065 \pm 0.0005$	<b><math>0.0063 \pm 0.0003</math></b>	$0.0069 \pm 0.0003$
	36-hour	$0.0076 \pm 0.0006$	<b><math>0.0067 \pm 0.0007</math></b>	$0.0070 \pm 0.0002$	$0.0073 \pm 0.0003$
CA09P	6-hour	$0.0167 \pm 0.0017$	$0.0107 \pm 0.0008$	<b><math>0.0103 \pm 0.0003</math></b>	$0.0104 \pm 0.0007$
	12-hour	$0.0192 \pm 0.0017$	$0.0199 \pm 0.0013$	$0.0145 \pm 0.0006$	<b><math>0.0143 \pm 0.0004</math></b>
	24-hour	$0.0267 \pm 0.0016$	$0.0222 \pm 0.0019$	<b><math>0.0192 \pm 0.0008</math></b>	$0.0212 \pm 0.0006$
	36-hour	$0.0284 \pm 0.0009$	$0.0278 \pm 0.0007$	<b><math>0.0240 \pm 0.0009</math></b>	$0.0259 \pm 0.0005$

Table 5: MAE of short-term predictions..

Data	Step	BiGRU	Cfg 1	Cfg 2	Cfg 3
ETTh1	6-hour	$0.1810 \pm 0.0306$	$0.0280 \pm 0.0106$	$0.0325 \pm 0.0034$	<b><math>0.0271 \pm 0.0026</math></b>
	12-hour	$0.1419 \pm 0.0339$	$0.0296 \pm 0.0133$	$0.0356 \pm 0.0025$	<b><math>0.0344 \pm 0.0021</math></b>
	24-hour	$0.0967 \pm 0.0234$	$0.0356 \pm 0.0120$	$0.0376 \pm 0.0042$	<b><math>0.0334 \pm 0.0029</math></b>
	36-hour	$0.1049 \pm 0.0239$	$0.0562 \pm 0.0129$	$0.0408 \pm 0.0011$	<b><math>0.0394 \pm 0.0021</math></b>
ETTh2	6-hour	$0.1415 \pm 0.0094$	$0.1017 \pm 0.0112$	<b><math>0.0749 \pm 0.0017</math></b>	$0.0752 \pm 0.0019$
	12-hour	$0.1237 \pm 0.0096$	$0.1004 \pm 0.0063$	$0.1012 \pm 0.0010$	<b><math>0.0988 \pm 0.0012</math></b>
	24-hour	$0.1352 \pm 0.0131$	$0.0822 \pm 0.0101$	<b><math>0.0590 \pm 0.0026</math></b>	$0.0591 \pm 0.0028$
	36-hour	$0.1486 \pm 0.0101$	$0.0909 \pm 0.0082$	$0.0923 \pm 0.0041$	<b><math>0.0825 \pm 0.0042</math></b>
C46207	6-hour	$0.0436 \pm 0.0022$	$0.0288 \pm 0.0018$	$0.0311 \pm 0.0023$	<b><math>0.0269 \pm 0.0016</math></b>
	12-hour	$0.0438 \pm 0.0019$	$0.0303 \pm 0.0020$	$0.0318 \pm 0.0030$	<b><math>0.0298 \pm 0.0028</math></b>
	24-hour	$0.0470 \pm 0.0009$	<b><math>0.0363 \pm 0.0017</math></b>	$0.0389 \pm 0.0020$	$0.0409 \pm 0.0019$
	36-hour	$0.0506 \pm 0.0008$	<b><math>0.0380 \pm 0.0024</math></b>	$0.0422 \pm 0.0037$	$0.0419 \pm 0.0016$
C46208	6-hour	$0.0469 \pm 0.0106$	$0.0334 \pm 0.0122$	$0.0329 \pm 0.0097$	<b><math>0.0325 \pm 0.0106</math></b>
	12-hour	$0.0485 \pm 0.0139$	$0.0601 \pm 0.0201$	<b><math>0.0443 \pm 0.0120</math></b>	$0.0452 \pm 0.0170$
	24-hour	$0.0468 \pm 0.0125$	<b><math>0.0407 \pm 0.0120</math></b>	$0.0451 \pm 0.0132$	$0.0494 \pm 0.0128$
	36-hour	$0.0518 \pm 0.0155$	<b><math>0.0441 \pm 0.0127</math></b>	$0.0480 \pm 0.0145$	$0.0448 \pm 0.0119$
CA06P	6-hour	$0.0459 \pm 0.0013$	$0.0447 \pm 0.0012$	$0.0442 \pm 0.0010$	<b><math>0.0439 \pm 0.0008</math></b>
	12-hour	$0.0473 \pm 0.0015$	<b><math>0.0451 \pm 0.0015</math></b>	$0.0464 \pm 0.0014$	$0.0458 \pm 0.0007$
	24-hour	$0.0540 \pm 0.0030$	$0.0526 \pm 0.0025$	$0.0499 \pm 0.0016$	<b><math>0.0497 \pm 0.0015</math></b>
	36-hour	$0.0562 \pm 0.0031$	$0.0566 \pm 0.0037$	<b><math>0.0531 \pm 0.0013</math></b>	$0.0536 \pm 0.0007$
CA09P	6-hour	$0.0770 \pm 0.0035$	$0.0626 \pm 0.0023$	<b><math>0.0628 \pm 0.0008</math></b>	$0.0632 \pm 0.0019$
	12-hour	$0.0800 \pm 0.0031$	$0.0797 \pm 0.0027$	$0.0726 \pm 0.0018$	<b><math>0.0719 \pm 0.0015</math></b>
	24-hour	$0.0912 \pm 0.0028$	$0.0856 \pm 0.0034$	<b><math>0.0793 \pm 0.0013</math></b>	$0.0821 \pm 0.0011$
	36-hour	$0.0959 \pm 0.0034$	$0.0909 \pm 0.0021$	<b><math>0.0892 \pm 0.0014</math></b>	$0.0913 \pm 0.0008$

Table 6: RMSE of short-term predictions..

Data	Step	BiGRU	Cfg 1	Cfg 2	Cfg 3
ETTh1	6-hour	$0.2251 \pm 0.0220$	$0.0490 \pm 0.0041$	$0.0458 \pm 0.0022$	<b><math>0.0346 \pm 0.0029</math></b>
	12-hour	$0.1769 \pm 0.0292$	$0.0539 \pm 0.0065$	$0.0448 \pm 0.0032$	<b><math>0.0436 \pm 0.0023</math></b>
	24-hour	$0.1349 \pm 0.0189$	$0.0663 \pm 0.0098$	$0.0479 \pm 0.0023$	<b><math>0.0458 \pm 0.0022</math></b>
	36-hour	$0.1521 \pm 0.0223$	$0.0721 \pm 0.0159$	$0.0523 \pm 0.0015$	<b><math>0.0510 \pm 0.0029</math></b>
ETTh2	6-hour	$0.1761 \pm 0.0123$	$0.1212 \pm 0.0125$	$0.0989 \pm 0.0010$	<b><math>0.0980 \pm 0.0010</math></b>
	12-hour	$0.1570 \pm 0.0112$	$0.1227 \pm 0.0078$	$0.1253 \pm 0.0069$	<b><math>0.1229 \pm 0.0057</math></b>
	24-hour	$0.1726 \pm 0.0147$	$0.1032 \pm 0.0121$	<b><math>0.0795 \pm 0.0026</math></b>	$0.0806 \pm 0.0031$
	36-hour	$0.1911 \pm 0.0116$	$0.1148 \pm 0.0105$	$0.1182 \pm 0.0045$	<b><math>0.1077 \pm 0.0046</math></b>
C46207	6-hour	$0.0602 \pm 0.0028$	<b><math>0.0402 \pm 0.0027</math></b>	$0.0424 \pm 0.0024$	$0.0412 \pm 0.0036$
	12-hour	$0.0615 \pm 0.0023$	<b><math>0.0423 \pm 0.0030</math></b>	$0.0458 \pm 0.0033$	$0.0436 \pm 0.0034$
	24-hour	$0.0689 \pm 0.0017$	$0.0518 \pm 0.0025$	$0.0574 \pm 0.0017$	<b><math>0.0504 \pm 0.0020</math></b>
	36-hour	$0.0736 \pm 0.0015$	<b><math>0.0543 \pm 0.0029</math></b>	$0.0648 \pm 0.0015$	$0.0566 \pm 0.0027$
C46208	6-hour	$0.0805 \pm 0.0268$	$0.0768 \pm 0.0143$	$0.0781 \pm 0.0019$	<b><math>0.0693 \pm 0.0152</math></b>
	12-hour	$0.0844 \pm 0.0393$	$0.0959 \pm 0.0192$	$0.0866 \pm 0.0017$	<b><math>0.0843 \pm 0.0231</math></b>
	24-hour	$0.0745 \pm 0.0051$	<b><math>0.0604 \pm 0.0102</math></b>	$0.0663 \pm 0.0023$	$0.0648 \pm 0.0147$
	36-hour	$0.0822 \pm 0.0159$	<b><math>0.0774 \pm 0.0187</math></b>	$0.0781 \pm 0.0013$	$0.0825 \pm 0.0133$
CA06P	6-hour	$0.0710 \pm 0.0018$	$0.0685 \pm 0.0019$	<b><math>0.0673 \pm 0.0014</math></b>	$0.0693 \pm 0.0014$
	12-hour	$0.0736 \pm 0.0015$	<b><math>0.0697 \pm 0.0014</math></b>	$0.0722 \pm 0.0020$	$0.0714 \pm 0.0014$
	24-hour	$0.0849 \pm 0.0034$	$0.0807 \pm 0.0029$	<b><math>0.0795 \pm 0.0018</math></b>	$0.0831 \pm 0.0018$
	36-hour	$0.0870 \pm 0.0036$	<b><math>0.0867 \pm 0.0038</math></b>	$0.0834 \pm 0.0015$	$0.0854 \pm 0.0018$
CA09P	6-hour	$0.1289 \pm 0.0066$	$0.1034 \pm 0.0039$	<b><math>0.1017 \pm 0.0016</math></b>	$0.1020 \pm 0.0034$
	12-hour	$0.1385 \pm 0.0061$	$0.1411 \pm 0.0046$	$0.1206 \pm 0.0024$	<b><math>0.1196 \pm 0.0017</math></b>
	24-hour	$0.1633 \pm 0.0049$	$0.1490 \pm 0.0064$	<b><math>0.1384 \pm 0.0031</math></b>	$0.1456 \pm 0.0021$
	36-hour	$0.1685 \pm 0.0027$	$0.1667 \pm 0.0021$	<b><math>0.1549 \pm 0.0030</math></b>	$0.1609 \pm 0.0016$

### 5.3 Long-term prediction

For long-term prediction, we developed a TIS-Informer model that was based on Informer [45] composed of an encoder and a decoder that both contain *ProbSparse* attention mechanism and 1-dimensional convolution layers. Figure 8 illustrates a single stack within the encoder of the Informer architecture. In the total loss function (Equation 47), we set the hyperparameter  $\lambda = 10.0$ , and both the topological loss and prediction loss are implemented using the  $L_2$  loss.

In the long-term prediction task, the model predicts all variables simultaneously, rather than selecting specific target variables. The prediction length  $t$  was selected from the set  $\{48, 96, 168, 336\}$ . We adopted a rolled training and testing strategy, where the input sequence  $\mathbf{x}_{1:L}$  is used to predict the next sequence  $\mathbf{x}_{L+1:L+t}$ . Subsequently, the input window shifts forward, using  $\mathbf{x}_{2:L+1}$  to predict  $\mathbf{x}_{L+2:L+t+1}$ , and this process continues throughout the time series. To maintain consistency, we set the prediction length equal to the sequence length of the input variables, i.e.,  $L = t$ . Additionally, historical information is provided to the decoder, with the context length set equal to the sequence length.

The training configuration consisted of 6 epochs and a batch size of 32. During each epoch, the model iterated over the entire shuffled training dataset, following the workflow shown in Figure 6(a). The encoder was configured with 3 layers, while the decoder utilized 2 layers. The topological feature embedder was designed similarly to the one developed for the short-term predictor. The Adam optimizer was utilized with a learning rate schedule that started at  $1 \times 10^{-4}$  for the first epoch. The learning rate was then progressively decreased over the

following epochs as follows:

1. Epoch 2:  $5 \times 10^{-5}$
2. Epoch 4:  $1 \times 10^{-5}$
3. Epoch 6:  $5 \times 10^{-6}$

We configured the *ProbSparse* attention mechanism with 8 heads and set the model dimension to 512 after embedding. The dropout rate was set to 0.05. We allocated 10% of the dataset for validation. Early stopping was implemented, triggering when the validation loss fails to improve for 7 consecutive epochs.

Also, to ensure robustness and reliability, the training and inference process was repeated 10 times for each dataset. The performance of the model was evaluated using the MSE, MAE, and RMSE, along with their standard deviations across the 10 runs. Tables 7, 8, and 9 present the evaluation results for six datasets using the metrics.

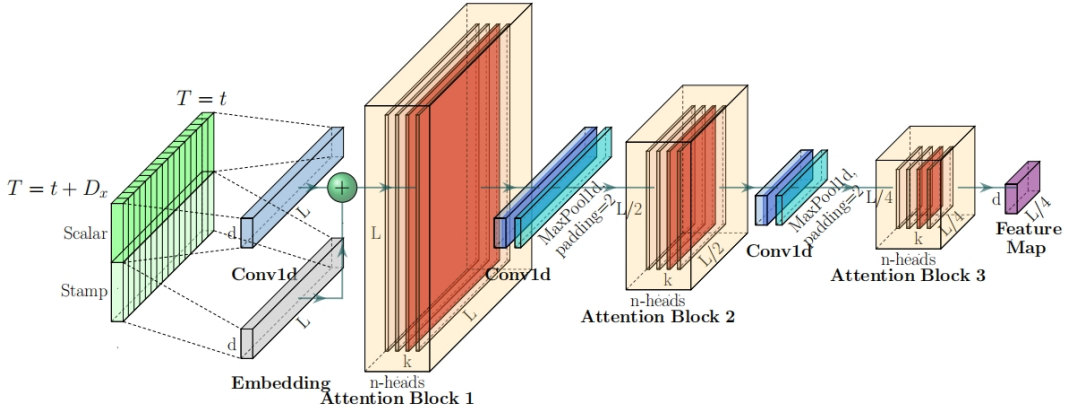


Figure 8: The single stack in Informer’s encoder. This figure is sourced from [45].

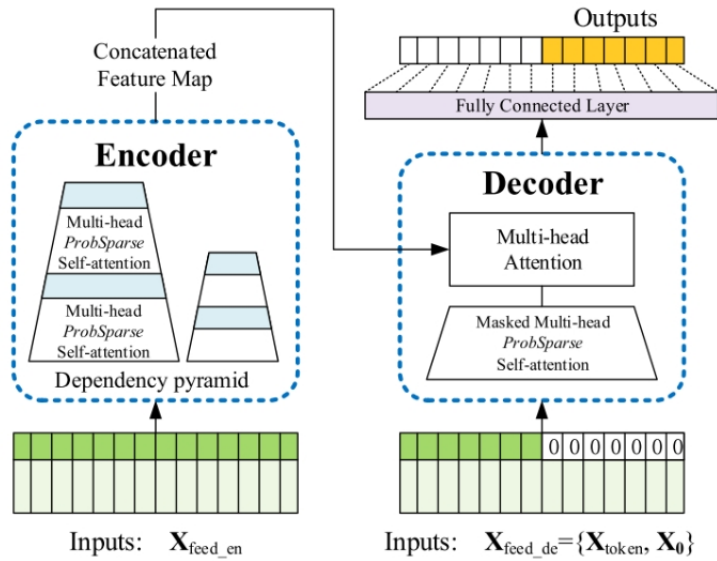


Figure 9: An overview of Informer’s architecture. This figure is sourced from [45].

Table 7: MSE of long-term predictions

Data	Step	Informer	Cfg 1	Cfg 2	Cfg 3
ETTh1	48-hour	0.7015 $\pm$ 0.0349	0.7130 $\pm$ 0.0251	0.6272 $\pm$ 0.0308	<b>0.6156 <math>\pm</math> 0.0396</b>
	96-hour	0.8589 $\pm$ 0.0472	0.8842 $\pm$ 0.0618	0.8448 $\pm$ 0.0417	<b>0.8362 <math>\pm</math> 0.0478</b>
	168-hour	1.0153 $\pm$ 0.0663	1.0368 $\pm$ 0.0694	0.9973 $\pm$ 0.0665	<b>0.9851 <math>\pm</math> 0.0552</b>
	336-hour	1.2172 $\pm$ 0.0718	1.2660 $\pm$ 0.0803	<b>1.1788 <math>\pm</math> 0.0511</b>	1.1831 $\pm$ 0.0669
ETTh2	48-hour	1.3523 $\pm$ 0.1748	1.3702 $\pm$ 0.1633	<b>1.2212 <math>\pm</math> 0.1023</b>	1.2902 $\pm$ 0.1784
	96-hour	3.5278 $\pm$ 0.3004	3.3055 $\pm$ 0.2039	3.2569 $\pm$ 0.3246	<b>2.7869 <math>\pm</math> 0.4847</b>
	168-hour	8.3987 $\pm$ 1.0804	7.6670 $\pm$ 0.8005	<b>6.6284 <math>\pm</math> 0.5160</b>	7.5388 $\pm$ 0.6844
	336-hour	3.0959 $\pm$ 0.3324	3.0901 $\pm$ 0.2526	<b>2.9105 <math>\pm</math> 0.2271</b>	3.0763 $\pm$ 0.2350
C46207	48-hour	0.5304 $\pm$ 0.0130	0.5010 $\pm$ 0.0134	0.4768 $\pm$ 0.0112	<b>0.4572 <math>\pm</math> 0.0154</b>
	96-hour	0.6710 $\pm$ 0.0127	0.6272 $\pm$ 0.0113	0.6015 $\pm$ 0.0106	<b>0.6009 <math>\pm</math> 0.0220</b>
	168-hour	0.7061 $\pm$ 0.0150	0.6880 $\pm$ 0.0135	0.6634 $\pm$ 0.0162	<b>0.6558 <math>\pm</math> 0.0279</b>
	336-hour	0.8031 $\pm$ 0.0142	0.7781 $\pm$ 0.0130	0.7702 $\pm$ 0.0117	<b>0.7640 <math>\pm</math> 0.0195</b>
C46208	48-hour	3.9525 $\pm$ 0.0517	3.6335 $\pm$ 0.0568	<b>3.2990 <math>\pm</math> 0.0487</b>	3.7708 $\pm$ 0.0984
	96-hour	4.1863 $\pm$ 0.0623	4.0343 $\pm$ 0.0212	<b>3.5295 <math>\pm</math> 0.0470</b>	4.0176 $\pm$ 0.0514
	168-hour	4.3533 $\pm$ 0.0349	4.0583 $\pm$ 0.0577	<b>3.7423 <math>\pm</math> 0.0455</b>	4.1276 $\pm$ 0.0323
	336-hour	4.1408 $\pm$ 0.0324	3.9453 $\pm$ 0.0339	<b>3.8007 <math>\pm</math> 0.0401</b>	3.8850 $\pm$ 0.0499
CA06P	48-hour	0.9734 $\pm$ 0.0243	0.9234 $\pm$ 0.0388	0.9721 $\pm$ 0.0113	<b>0.9056 <math>\pm</math> 0.0186</b>
	96-hour	1.1446 $\pm$ 0.0422	<b>0.9889 <math>\pm</math> 0.0364</b>	1.0939 $\pm$ 0.0165	1.1016 $\pm$ 0.0114
	168-hour	1.1584 $\pm$ 0.0228	<b>1.0109 <math>\pm</math> 0.0220</b>	1.0857 $\pm$ 0.0189	1.1362 $\pm$ 0.0261
	336-hour	1.1975 $\pm$ 0.0201	<b>1.0884 <math>\pm</math> 0.0221</b>	1.1335 $\pm$ 0.0164	1.1684 $\pm$ 0.0197
CA09P	48-hour	2.3177 $\pm$ 0.0910	2.2973 $\pm$ 0.0817	<b>2.2784 <math>\pm</math> 0.0507</b>	2.3004 $\pm$ 0.0628
	96-hour	2.3736 $\pm$ 0.0566	<b>2.3002 <math>\pm</math> 0.0479</b>	2.3407 $\pm$ 0.0420	2.3615 $\pm$ 0.0416
	168-hour	2.4504 $\pm$ 0.0465	2.3395 $\pm$ 0.0502	<b>2.3001 <math>\pm</math> 0.0454</b>	2.4145 $\pm$ 0.0520
	336-hour	2.7255 $\pm$ 0.0469	2.6630 $\pm$ 0.0445	<b>2.5998 <math>\pm</math> 0.0430</b>	2.6436 $\pm$ 0.0415

Table 8: MAE of long-term predictions.

Data	Step	Informer	Cfg 1	Cfg 2	Cfg 3
ETTh1	48-hour	0.6109 $\pm$ 0.0315	0.6171 $\pm$ 0.0335	0.5894 $\pm$ 0.0396	<b>0.5862 <math>\pm</math> 0.0391</b>
	96-hour	0.7725 $\pm$ 0.0194	0.7812 $\pm$ 0.0325	0.7535 $\pm$ 0.0297	<b>0.7512 <math>\pm</math> 0.0323</b>
	168-hour	0.7947 $\pm$ 0.0473	0.8019 $\pm$ 0.0347	0.7829 $\pm$ 0.0384	<b>0.7795 <math>\pm</math> 0.0359</b>
	336-hour	0.9416 $\pm$ 0.0541	0.9620 $\pm$ 0.0559	<b>0.9311 <math>\pm</math> 0.0533</b>	0.9347 $\pm$ 0.0506
ETTh2	48-hour	0.8452 $\pm$ 0.0696	0.8792 $\pm$ 0.1102	<b>0.8339 <math>\pm</math> 0.0389</b>	0.8482 $\pm$ 0.0314
	96-hour	1.5565 $\pm$ 0.0627	1.4120 $\pm$ 0.0587	1.4304 $\pm$ 0.0929	<b>1.3380 <math>\pm</math> 0.0592</b>
	168-hour	2.5880 $\pm$ 0.2019	2.2880 $\pm$ 0.1494	<b>1.8256 <math>\pm</math> 0.1662</b>	2.2446 $\pm$ 0.1410
	336-hour	1.5299 $\pm$ 0.0657	1.4308 $\pm$ 0.0495	<b>1.3504 <math>\pm</math> 0.0503</b>	1.5007 $\pm$ 0.0611
C46207	48-hour	0.5162 $\pm$ 0.0076	0.5003 $\pm$ 0.0055	0.5100 $\pm$ 0.0065	<b>0.4981 <math>\pm</math> 0.0089</b>
	96-hour	0.5904 $\pm$ 0.0047	0.5737 $\pm$ 0.0035	<b>0.5483 <math>\pm</math> 0.0049</b>	0.5547 $\pm$ 0.0085
	168-hour	0.6182 $\pm$ 0.0076	0.5889 $\pm$ 0.0102	<b>0.5514 <math>\pm</math> 0.0052</b>	0.5651 $\pm$ 0.0112
	336-hour	0.6777 $\pm$ 0.0074	0.6530 $\pm$ 0.0081	<b>0.6334 <math>\pm</math> 0.0079</b>	0.6377 $\pm$ 0.0090
C46208	48-hour	0.6787 $\pm$ 0.0085	0.6527 $\pm$ 0.0068	<b>0.6326 <math>\pm</math> 0.0072</b>	0.6496 $\pm$ 0.0073
	96-hour	0.7344 $\pm$ 0.0055	<b>0.7085 <math>\pm</math> 0.0056</b>	0.7104 $\pm$ 0.0039	0.7155 $\pm$ 0.0040
	168-hour	0.7657 $\pm$ 0.0057	0.7441 $\pm$ 0.0052	<b>0.7314 <math>\pm</math> 0.0048</b>	0.7496 $\pm$ 0.0073
	336-hour	0.7758 $\pm$ 0.0037	0.7453 $\pm$ 0.0042	<b>0.7366 <math>\pm</math> 0.0045</b>	0.7600 $\pm$ 0.0038
CA06P	48-hour	0.6676 $\pm$ 0.0060	0.6550 $\pm$ 0.0058	0.6699 $\pm$ 0.0064	<b>0.6477 <math>\pm</math> 0.0051</b>
	96-hour	0.7704 $\pm$ 0.0143	0.7540 $\pm$ 0.0121	<b>0.7271 <math>\pm</math> 0.0041</b>	0.7363 $\pm$ 0.0094
	168-hour	0.7946 $\pm$ 0.0116	0.7605 $\pm$ 0.0114	0.7664 $\pm$ 0.0056	<b>0.7538 <math>\pm</math> 0.0110</b>
	336-hour	0.8118 $\pm$ 0.0057	<b>0.7722 <math>\pm</math> 0.0091</b>	0.7802 $\pm$ 0.0085	0.7904 $\pm$ 0.0091
CA09P	48-hour	<b>0.7835 <math>\pm</math> 0.0148</b>	0.7868 $\pm$ 0.0139	0.7844 $\pm$ 0.0166	0.7875 $\pm$ 0.0109
	96-hour	0.8462 $\pm$ 0.0131	<b>0.8260 <math>\pm</math> 0.0115</b>	0.8473 $\pm$ 0.0299	0.8276 $\pm$ 0.0197
	168-hour	0.8756 $\pm$ 0.0153	0.8595 $\pm$ 0.0177	<b>0.8522 <math>\pm</math> 0.0162</b>	0.8668 $\pm$ 0.0043
	336-hour	0.9222 $\pm$ 0.0185	0.9163 $\pm$ 0.0174	<b>0.9007 <math>\pm</math> 0.0207</b>	0.9104 $\pm$ 0.0172

Table 9: RMSE of long-term predictions.

Data	Step	Informer	Cfg 1	Cfg 2	Cfg 3
ETTh1	48-hour	0.8376 $\pm$ 0.0208	0.8444 $\pm$ 0.0149	0.7920 $\pm$ 0.0194	<b>0.7846 <math>\pm</math> 0.0252</b>
	96-hour	0.9268 $\pm$ 0.0255	0.9403 $\pm$ 0.0329	0.9191 $\pm$ 0.0227	<b>0.9144 <math>\pm</math> 0.0261</b>
	168-hour	1.0076 $\pm$ 0.0329	1.0182 $\pm$ 0.0341	0.9986 $\pm$ 0.0333	<b>0.9925 <math>\pm</math> 0.0278</b>
	336-hour	1.1033 $\pm$ 0.0325	1.1252 $\pm$ 0.0357	<b>1.0857 <math>\pm</math> 0.0235</b>	1.0877 $\pm$ 0.0308
ETTh2	48-hour	1.1629 $\pm$ 0.0752	1.1706 $\pm$ 0.0698	<b>1.1051 <math>\pm</math> 0.0463</b>	1.1359 $\pm$ 0.0785
	96-hour	1.8793 $\pm$ 0.0426	1.8181 $\pm$ 0.0568	1.8052 $\pm$ 0.0499	<b>1.6699 <math>\pm</math> 0.1448</b>
	168-hour	2.8981 $\pm$ 0.0643	2.7690 $\pm$ 0.1447	<b>2.5746 <math>\pm</math> 0.0390</b>	2.7457 $\pm$ 0.0454
	336-hour	1.7595 $\pm$ 0.0534	1.7587 $\pm$ 0.0409	<b>1.7060 <math>\pm</math> 0.0391</b>	1.7545 $\pm$ 0.0382
C46207	48-hour	0.7283 $\pm$ 0.0089	0.7078 $\pm$ 0.0095	0.6905 $\pm$ 0.0117	<b>0.6762 <math>\pm</math> 0.0168</b>
	96-hour	0.8191 $\pm$ 0.0078	0.7920 $\pm$ 0.0071	0.7757 $\pm$ 0.0068	<b>0.7753 <math>\pm</math> 0.0142</b>
	168-hour	0.8403 $\pm$ 0.0089	0.8295 $\pm$ 0.0081	0.8145 $\pm$ 0.0099	<b>0.8109 <math>\pm</math> 0.0170</b>
	336-hour	0.8962 $\pm$ 0.0079	0.8821 $\pm$ 0.0074	0.8777 $\pm$ 0.0076	<b>0.8742 <math>\pm</math> 0.0128</b>
C46208	48-hour	1.9881 $\pm$ 0.0130	1.9062 $\pm$ 0.0078	<b>1.8163 <math>\pm</math> 0.0134</b>	1.9411 $\pm$ 0.0131
	96-hour	2.0349 $\pm$ 0.0080	2.0090 $\pm$ 0.0053	<b>1.8797 <math>\pm</math> 0.0125</b>	2.0050 $\pm$ 0.0064
	168-hour	2.0460 $\pm$ 0.0152	2.0157 $\pm$ 0.0143	<b>1.9352 <math>\pm</math> 0.0118</b>	2.0316 $\pm$ 0.0040
	336-hour	2.0865 $\pm$ 0.0084	1.9863 $\pm$ 0.0085	<b>1.9495 <math>\pm</math> 0.0103</b>	1.9699 $\pm$ 0.0063
CA06P	48-hour	0.9866 $\pm$ 0.0123	0.9602 $\pm$ 0.0202	0.9859 $\pm$ 0.0057	<b>0.9511 <math>\pm</math> 0.0103</b>
	96-hour	1.0699 $\pm$ 0.0197	<b>0.9944 <math>\pm</math> 0.0183</b>	1.0459 $\pm$ 0.0075	1.0491 $\pm$ 0.0052
	168-hour	1.0763 $\pm$ 0.0106	<b>1.0054 <math>\pm</math> 0.0109</b>	1.0415 $\pm$ 0.0087	1.0652 $\pm$ 0.0115
	336-hour	1.0943 $\pm$ 0.0092	<b>1.0433 <math>\pm</math> 0.0106</b>	1.0655 $\pm$ 0.0072	1.0819 $\pm$ 0.0084
CA09P	48-hour	1.5224 $\pm$ 0.0299	1.5166 $\pm$ 0.0355	<b>1.5094 <math>\pm</math> 0.0170</b>	1.5167 $\pm$ 0.0207
	96-hour	1.5406 $\pm$ 0.0184	<b>1.5172 <math>\pm</math> 0.0158</b>	1.5306 $\pm$ 0.0137	1.5373 $\pm$ 0.0136
	168-hour	1.5654 $\pm$ 0.0149	1.5295 $\pm$ 0.0161	<b>1.5166 <math>\pm</math> 0.0150</b>	1.5530 $\pm$ 0.0151
	336-hour	1.6509 $\pm$ 0.0142	1.6319 $\pm$ 0.0133	<b>1.6124 <math>\pm</math> 0.0133</b>	1.6259 $\pm$ 0.0121

## 6 Ablation Study

### 6.1 Comparison of computational time

To compare the computational time between the conventional chain of operations for computing topological features (referred to as Configuration 0 in this study) and the developed models, we conducted experiments using simulated data. The synthetic data is generated using a sine wave model [69] with randomized frequency and phase for each dimension. Specifically, for each time series sample  $i$  and each dimension  $k$ , the frequency  $f_k$  and phase  $\phi_k$  are independently sampled from a uniform distribution:

$$f_k \sim U(0, 0.1), \quad \phi_k \sim U(0, 0.1) \quad (51)$$

The value of the  $k$ -th dimension at time step  $j$  is then calculated using the sine function:

$$X_{i,k}(j) = \sin(f_k \cdot j + \phi_k), \quad j = 0, 1, \dots, L - 1 \quad (52)$$

To ensure all values fall within the range  $[0, 1]$ , the sine values are normalized as follows:

$$X_{i,k}(j) = \frac{\sin(f_k \cdot j + \phi_k) + 1}{2} \quad (53)$$

In the experiment, we set the dimension of data to 10, so that each time step consists of 10 values corresponding to 10 independent sine waves. This results in a multidimensional time series of shape  $(L, 10)$  for each sequence.

The experiments were performed on a machine equipped with an Intel(R) Xeon(R) Platinum 8474C and an Nvidia RTX 4090D GPU. To ensure a fair comparison, the experiments were restricted to using one CPU core, 8 CPU cores and one GPU. This is due to the following reasons and considerations:

1. Consistency: It provides a consistent baseline for comparison, ensuring that differences in computational time are due to the models themselves and not due to varying hardware resources.
2. Scalability: The results can be easily scaled to predict performance on multi-core or multi-GPU setups.
3. Reproducibility: Limiting the resources enhances the reproducibility of the experiment.

We selected Configuration 2 as the model to compare against Configuration 0. The sequence lengths tested were  $\{6, 12, 24, 36, 48, 96, 168, 336\}$ . For each sequence length, we measured the time required by both models to generate data with a batch size of 128. For long sequences (168 and 336), we generated 100 batch size topological features and recorded the corresponding computational times. Due to the highly linear trend observed in the curves, these recorded times were used to approximate the computational times for subsequent experiments.

Table 10 presents a performance comparison of Configuration 0 using 1 core and 8 cores, Cfg 0 (1 core) and Cfg 0 (8 cores), for different sequence lengths. It also calculates the growing rate (%) for each setting.

Figure 10 presents the cumulative times required by Configuration 0 (1 core) and Configuration 2 to generate topological features across various sequence lengths. In all subfigures, the curves for Configuration 2 intersect the y-axis at a non-zero point, reflecting the initial training time needed to pre-train the models. This initial cost remains constant regardless of the sequence length since the models are trained once and then reused for all sequences. In contrast, the curves for Configuration 0 show a linear increase in cumulative time as the sequence length increases, indicating a direct dependency on the input size. This trend highlights the inefficiency of Configuration 0 for longer sequences. The steep slope demonstrates that the conventional chain of operations becomes increasingly time-consuming as the data volume grows.

Figure 11 compares the computational times of Configuration 0 (8 cores) and Configuration 2 for generating topological features for one batch size across different sequence lengths. In Figure 11, the x-axis represents the sequence length, while the y-axis shows the logarithmic scale of the time (in seconds) required to generate one batch of topological features. The curves depict the mean computational times, with the variances forming the upper and lower boundaries.

Table 10: Configuration Times and Variances for Different Prediction Lengths (in Seconds)

Sequence Length	Cfg 0 (1 core) (s)	Cfg 0 (8 cores) (s)	Growing rate (1 core) (%)	Growing rate (8 cores) (%)
6	1.0376	1.0227	-	-
12	1.1816	1.0047	13.88	-1.76
24	2.6881	2.0452	127.47	103.58
36	5.9523	2.4452	121.47	19.57
48	9.7901	4.4761	64.42	83.09
96	60.7570	9.0857	520.67	102.92
168	258.5819	32.9466	325.54	262.57
336	1455.5820	242.8681	462.91	637.07

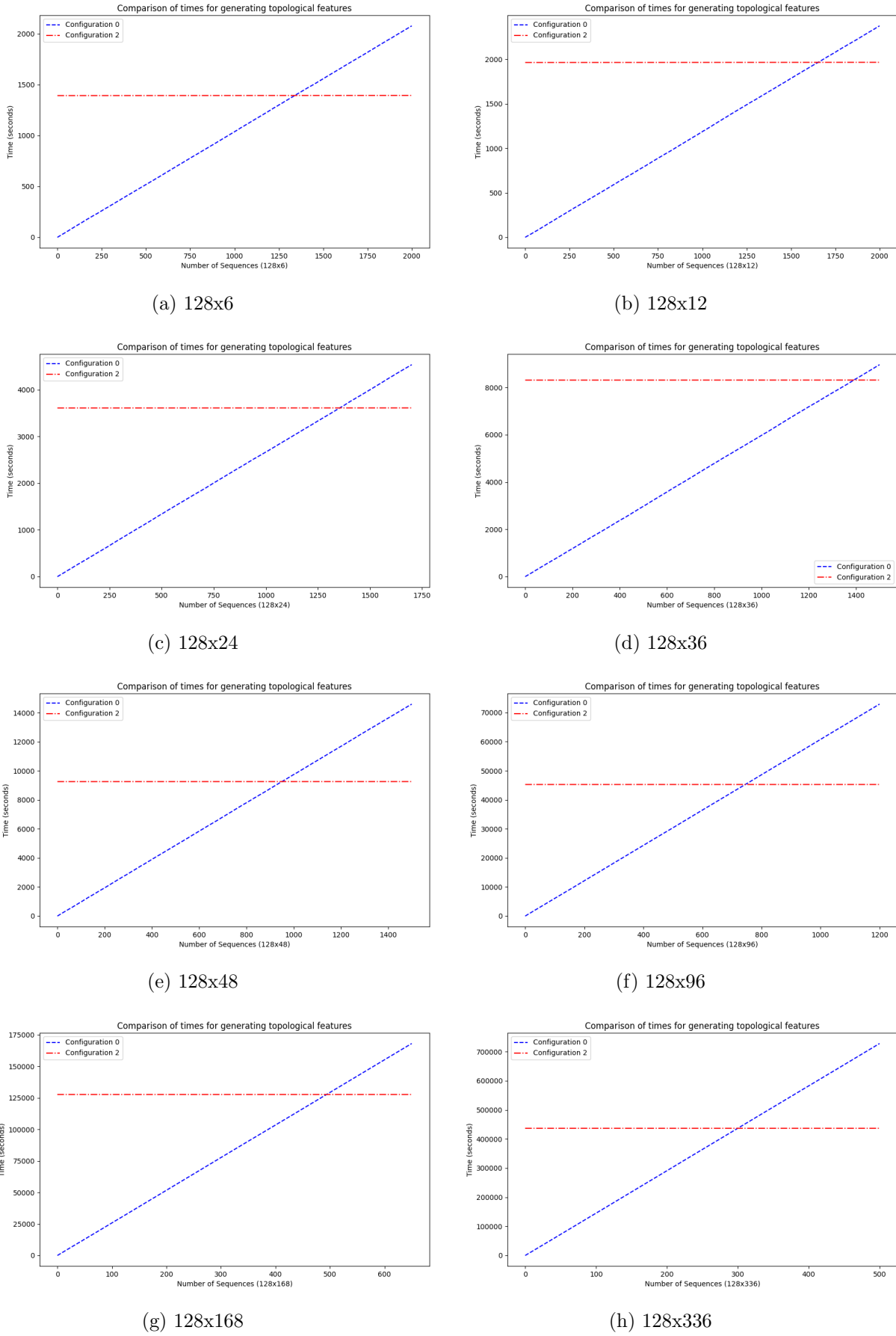


Figure 10: Comparison of Times for Different Configurations

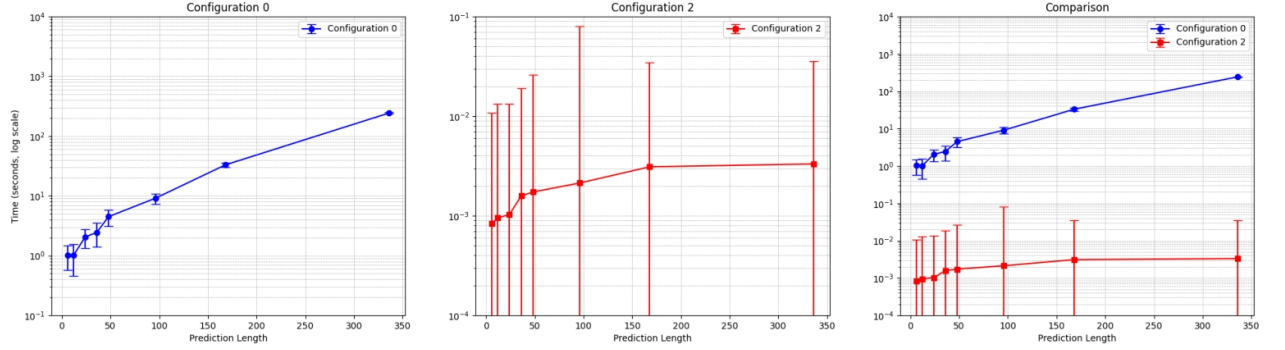


Figure 11: Sequence Comparison

## 6.2 Comparison of complex types

Table 11: Comparative analysis of prediction accuracy using different complex types.

Metric	Step	Rips	Weighted	Cubical	Cech
MSE	48-hour	$0.7130 \pm 0.0251$	<b><math>0.6643 \pm 0.0561</math></b>	$0.7680 \pm 0.0801$	$0.8064 \pm 0.0827$
	96-hour	$0.8842 \pm 0.0618$	<b><math>0.8808 \pm 0.0297</math></b>	$0.9014 \pm 0.0560$	$0.9880 \pm 0.0578$
	168-hour	$1.0368 \pm 0.0694$	<b><math>1.0110 \pm 0.0787</math></b>	$1.0550 \pm 0.0923$	$1.1379 \pm 0.0946$
	336-hour	$1.2660 \pm 0.0803$	<b><math>1.2255 \pm 0.0506</math></b>	$1.3993 \pm 0.0871$	$1.4943 \pm 0.0849$
MAE	48-hour	$0.6171 \pm 0.0335$	<b><math>0.6108 \pm 0.0392</math></b>	$0.6327 \pm 0.0484$	$0.6643 \pm 0.0521$
	96-hour	$0.7812 \pm 0.0325$	<b><math>0.7368 \pm 0.0152</math></b>	$0.7508 \pm 0.0340$	$0.8229 \pm 0.0351$
	168-hour	$0.8019 \pm 0.0347$	<b><math>0.7921 \pm 0.0443</math></b>	$0.8293 \pm 0.0460$	$0.8944 \pm 0.0471$
	336-hour	$0.9620 \pm 0.0559$	<b><math>0.9542 \pm 0.0370</math></b>	$0.9702 \pm 0.0398$	$1.0361 \pm 0.0434$
RMSE	48-hour	$0.8444 \pm 0.0149$	<b><math>0.8150 \pm 0.0344</math></b>	$0.8764 \pm 0.0457$	$0.8980 \pm 0.0460$
	96-hour	$0.9403 \pm 0.0329$	<b><math>0.9385 \pm 0.0258</math></b>	$0.9494 \pm 0.0295$	$0.9940 \pm 0.0291$
	168-hour	$1.0182 \pm 0.0341$	<b><math>1.0055 \pm 0.0391</math></b>	$1.0271 \pm 0.0449$	$1.0667 \pm 0.0443$
	336-hour	$1.1252 \pm 0.0357$	<b><math>1.1113 \pm 0.0320</math></b>	$1.1829 \pm 0.0368$	$1.2224 \pm 0.0347$
Count	-	1	11	0	0

We conducted a comparative analysis of different complex types to evaluate their impact on prediction accuracy. Specifically, we examined four widely used complex types: the Vietoris-Rips complex (Rips) (Definition 2), the weighted Vietoris-Rips complex (Weighted) (Definition 3), the Cubical complex (Definition 4), and the Cech complex (Definition 5). Long-term predictions were made for steps of 48, 96, 168, and 336 hours. The number of nearest neighbors in Weighted Vietoris-Rips complex was set to 3. Performance was assessed using three metrics: MSE, MAE, and RMSE. The results are presented in Table 11 and illustrated in Figure 12. All training details, including those for the network  $\text{Net}_\theta$  and the TIS-Informer, were kept consistent, with only the types of complexes used for topological feature engineering varying.

The results in Table 11 indicate that the weighted Vietoris-Rips complex consistently achieved the lowest error rates across most metrics and prediction steps, highlighting its superior predictive performance. Conversely, the cech complex generally exhibited the highest error rates, suggesting relatively lower accuracy in long-term predictions. The cubical complex and Vietoris-Rips complex showed intermediate performance, with the cubical complex slightly outperforming the Vietoris-Rips complex in a few cases. Figure 12 illustrates the comparative analysis. Each row corresponds to a prediction step, while each column represents a metric.

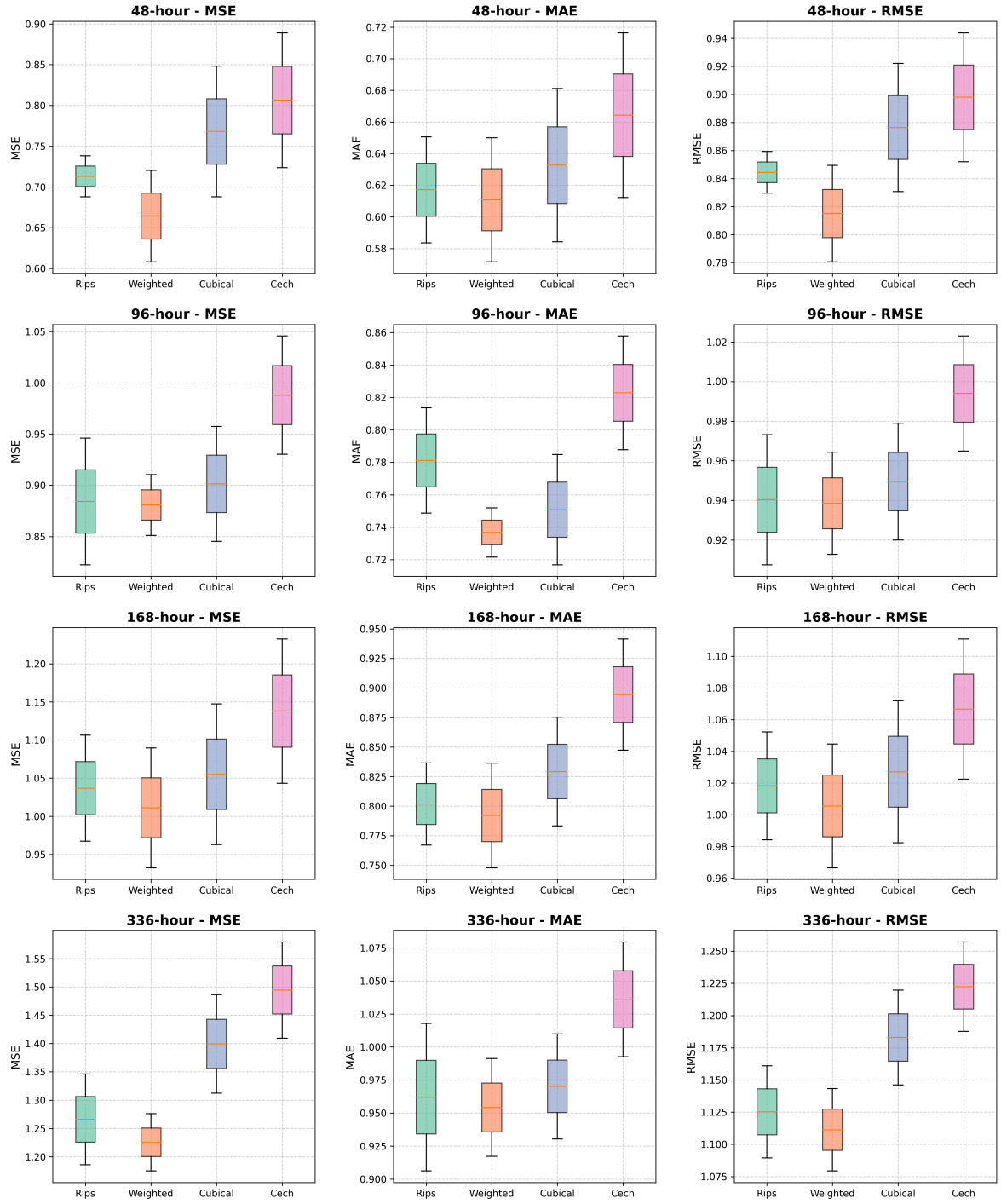


Figure 12: Box plots displaying comparative analysis of prediction accuracy across four complex types.

### 6.3 Impact of the discriminator on topological feature learning

We explored the role of the discriminator, specifically its function within the GAN framework, in learning topological features. Our focus was on how adopting the GAN framework enables the generator to capture the underlying distribution of these features more effectively. To measure the proximity of distributions, we employed t-SNE (t-Distributed Stochastic Neighbor Embedding) [70], a powerful machine learning algorithm for dimensionality reduction and visualization.

In our study, we mapped the topological features from a high-dimensional space to a 2-dimensional space as follows:

$$\text{t-SNE} : \mathbb{R}^{12} \rightarrow \mathbb{R}^2, \quad (54)$$

facilitating easier visualization and a better understanding of the data’s structure. Broadly speaking, when two distributions are close or similar, their low-dimensional representations generated by t-SNE tend to overlap significantly. Conversely, when the distributions differ substantially, their representations are well-separated [71].

We selected sequences from the set  $\{24, 36, 48, 96\}$  and developed two types of topological feature generators  $\text{Net}_\theta$ . One generator was trained within the GAN framework under the supervision of a discriminator, while the other was trained independently. Both generators and the discriminator followed the architectures of Configuration 3. All training parameters, including learning rate, optimizer type, and other hyperparameters, were kept consistent. After training, we generated 1000 samples of topological features using each generator and compared them to the true features using t-SNE. The comparison results are presented in Figure 13.

Figure 13 presents t-SNE visualizations comparing the distributions of true topological features and those generated by two types of generators: one trained without a discriminator (left column) and the other trained with a discriminator (right column). Four sequence lengths were analyzed: 24, 36, 48, and 96, corresponding to rows (a-b), (c-d), (e-f), and (g-h), respectively. In each subplot, green squares represent true topological features, while red triangles indicate synthetic features generated by the corresponding model. Results from the generator trained without a discriminator are shown in the left column (a, c, e, g), whereas those from the generator trained within the GAN framework are displayed in the right column (b, d, f, h). This arrangement highlights the impact of the discriminator on the generator’s ability to capture the underlying distribution of the topological features.

## 7 Discussion

### 7.1 Limitations and Future Research

1. The topological feature extractor  $\text{Net}_\theta$  is designed to capture the deterministic mapping  $f : \mathcal{X} \rightarrow \mathcal{T}$ , which is not data-specific (here, data-specific refers to a model that is trained or optimized for a particular type of data or dataset, rather than being generalizable to all types of input data). Therefore, it is possible to develop a  $\text{Net}_\theta$  that is also data-agnostic, capable of processing any type of data and any sequence, mapping them into a subspace of  $\mathcal{T}$ . In our experiments, however, we feed  $\text{Net}_\theta$  a broad range of data and find that data-specific and sequence-specific instances of  $\text{Net}_\theta$  outperform their non-specific counterparts. This may be due to several factors. First, the variance in the data fed to the network might not be large enough for the model to effectively learn the underlying mapping. Second, according to the Universal Approximation Theorem [72], the network architectures themselves may not be sufficiently complex to capture the underlying mapping in a generalizable way. Future work could explore expanding the training data to include a broader range of variations or developing more expressive network architectures to improve generalization across different types of data. Additionally, investigating adaptive mechanisms that allow  $\text{Net}_\theta$  to dynamically adjust to different data distributions could further enhance its performance.
2. In this work, we use RNNs to construct  $\text{Net}_\theta$  and extract intermediate representations as hidden states. However, probabilistic methods may provide better learning capabilities. For instance, these representations can be modeled as an invertible flow, such as Real NVP [73], Masked Autoregressive Flows [74], or a denoising diffusion process [68]. By

leveraging Real NVP, for example, the network can be optimized using:

$$\log p(\mathcal{X}) = \log p(\mathcal{T}) + \sum_{i=1}^K \log \left| \det \left( \frac{\partial \mathcal{Z}_i}{\partial \mathcal{Z}_{i-1}} \right) \right|. \quad (55)$$

This enables more effective density estimation and representation learning through invertible transformations. This presents a promising direction for future research, where exploring probabilistic approaches such as invertible flows could further enhance the effectiveness of topological feature extraction and representation learning.

3. In this work, we embedded the time series into a three-dimensional phase space with a time delay of  $\tau = 1$ . This choice is based on the observation that high-dimensional topological holes or voids rarely exist, except in a few long-sequence time series. Additionally, constructing complexes such as the Vietoris-Rips complex has polynomial time complexity with respect to the data dimension. However, this challenge can be addressed using dimensionality reduction techniques that preserve significant topological information, such as the Mapper method [75]. Future work could explore adaptive embedding strategies that dynamically adjust the phase space dimension based on the complexity of the time series.

## 8 Conclusion

This study explored the integration of Topological Data Analysis (TDA) with time-series prediction by introducing the Topological Information Supervised (TIS) Prediction framework. Building on the power of TDA to extract meaningful features from complex data, we leveraged conditional generative adversarial networks (CGANs) to synthesize and integrate topological features, preserving their distribution while significantly enhancing predictive accuracy. The proposed approach addressed the challenges of computational bottlenecks and deterministic pipelines in traditional TDA by generating flexible and generalized topological representations.

By embedding these features into advanced forecasting architectures, including TIS-BiGRU and TIS-Informer, the framework effectively captured both short-term and long-term temporal dependencies. Experimental results validated the superior performance of the TIS models compared to conventional predictors, highlighting the impact of incorporating topological information on predictive accuracy and robustness. The use of hybrid loss functions, combining prediction loss and topological consistency loss, demonstrated the model's capability to maintain high-level topological structures and internal dynamics.

Despite the promising outcomes, limitations in computational efficiency, potential biases in synthetic feature generation, and domain-specific applicability highlight areas for future exploration. Addressing these challenges and extending the framework's generalizability could further advance the field of TDA-based time-series prediction. This study not only contributes to the evolving landscape of predictive modeling but also opens new avenues for utilizing topological features in deep learning architectures, paving the way for more robust and interpretable machine learning solutions.

## References

- [1] D. Liang, S. Xia, X. Zhang, and W. Zhang, “Analysis of brain functional connectivity neural circuits in children with autism based on persistent homology,” *Frontiers in Human Neuroscience*, vol. 15, p. 745671, 2021.
- [2] A. E. Sizemore, C. Giusti, A. Kahn, J. M. Vettel, R. F. Betzel, and D. S. Bassett, “Cliques and cavities in the human connectome,” *Journal of Computational Neuroscience*, vol. 44, no. 1, pp. 115–145, 2018.

- [3] O. Vipond, J. A. Bull, P. S. Macklin, U. Tillmann, C. W. Pugh, H. M. Byrne, and H. A. Harrington, “Multiparameter persistent homology landscapes identify immune cell spatial patterns in tumors,” *Proceedings of the National Academy of Sciences*, vol. 118, no. 41, p. e2102166118, 2021.
- [4] N. Byrne, J. R. Clough, I. Valverde, G. Montana, and A. P. King, “A persistent homology-based topological loss for cnn-based multiclass segmentation of cmr,” *IEEE transactions on medical imaging*, vol. 42, no. 1, pp. 3–14, 2022.
- [5] H. Masoomy, B. Askari, S. Tajik, A. K. Rizi, and G. R. Jafari, “Topological analysis of interaction patterns in cancer-specific gene regulatory network: persistent homology approach,” *Scientific Reports*, vol. 11, no. 1, p. 16414, 2021.
- [6] R. Turkes, G. F. Montufar, and N. Otter, “On the effectiveness of persistent homology,” *Advances in Neural Information Processing Systems*, vol. 35, pp. 35432–35448, 2022.
- [7] M. Hajij, G. Zamzmi, and F. Batayneh, “Tda-net: fusion of persistent homology and deep learning features for covid-19 detection from chest x-ray images,” in *2021 43rd Annual International Conference of the IEEE Engineering in Medicine & Biology Society (EMBC)*, pp. 4115–4119, IEEE, 2021.
- [8] N. F. S. Zulkepli, M. S. M. Noorani, F. A. Razak, M. Ismail, and M. A. Alias, “Hybridization of hierarchical clustering with persistent homology in assessing haze episodes between air quality monitoring stations,” *Journal of environmental management*, vol. 306, p. 114434, 2022.
- [9] Y.-M. Chung, C.-S. Hu, Y.-L. Lo, and H.-T. Wu, “A persistent homology approach to heart rate variability analysis with an application to sleep-wake classification,” *Frontiers in physiology*, vol. 12, p. 637684, 2021.
- [10] S. Choe and S. Ramanna, “Cubical homology-based machine learning: An application in image classification,” *Axioms*, vol. 11, no. 3, p. 112, 2022.
- [11] Z. Lin, N. F. S. Zulkepli, M. S. M. Kasihmuddin, and R. Gobithaasan, “Hybridizing persistent homology and machine learning for oceanographic time series,” *Journal of Water and Climate Change*, p. jwc2025645, 2025.
- [12] I. Obayashi, T. Nakamura, and Y. Hiraoka, “Persistent homology analysis for materials research and persistent homology software: Homcloud,” *journal of the physical society of japan*, vol. 91, no. 9, p. 091013, 2022.
- [13] P. Corcoran and C. B. Jones, “Topological data analysis for geographical information science using persistent homology,” *International Journal of Geographical Information Science*, vol. 37, no. 3, pp. 712–745, 2023.
- [14] S. S. Sørensen, T. Du, C. A. Biscio, L. Fajstrup, and M. M. Smedskjaer, “Persistent homology: A tool to understand medium-range order glass structure,” *Journal of Non-Crystalline Solids: X*, vol. 16, p. 100123, 2022.
- [15] E. U. Samani and A. G. Banerjee, “Persistent homology meets object unity: Object recognition in clutter,” *IEEE Transactions on Robotics*, vol. 40, pp. 886–902, 2023.
- [16] E. Baitinger and S. Flegel, “The better turbulence index? forecasting adverse financial markets regimes with persistent homology,” *Financial Markets and Portfolio Management*, vol. 35, no. 3, pp. 277–308, 2021.

- [17] P. T.-W. Yen and S. A. Cheong, “Using topological data analysis (tda) and persistent homology to analyze the stock markets in singapore and taiwan,” *Frontiers in Physics*, vol. 9, p. 572216, 2021.
- [18] M. S. Ismail, M. S. M. Noorani, M. Ismail, F. A. Razak, and M. A. Alias, “Early warning signals of financial crises using persistent homology,” *Physica A: Statistical Mechanics and its Applications*, vol. 586, p. 126459, 2022.
- [19] S. Rudkin, W. Qiu, and P. Dłotko, “Uncertainty, volatility and the persistence norms of financial time series,” *Expert Systems with Applications*, vol. 223, p. 119894, 2023.
- [20] K. He, J. Shi, and H. Fang, “Bifurcation and chaos analysis of a fractional-order delay financial risk system using dynamic system approach and persistent homology,” *Mathematics and Computers in Simulation*, vol. 223, pp. 253–274, 2024.
- [21] Y. Wei, J. Watada, and Z. Wang, “Topology unveiled: A new horizon for economic and financial modeling,” *Mathematics*, vol. 13, no. 2, p. 325, 2025.
- [22] N. Otter, M. A. Porter, U. Tillmann, P. Grindrod, and H. A. Harrington, “A roadmap for the computation of persistent homology,” *EPJ Data Science*, vol. 6, pp. 1–38, 2017.
- [23] M. E. Aktas, E. Akbas, and A. E. Fatmaoui, “Persistence homology of networks: methods and applications,” *Applied Network Science*, vol. 4, no. 1, pp. 1–28, 2019.
- [24] C. S. Pun, S. X. Lee, and K. Xia, “Persistent-homology-based machine learning: a survey and a comparative study,” *Artificial Intelligence Review*, vol. 55, no. 7, pp. 5169–5213, 2022.
- [25] Y. Skaf and R. Laubenbacher, “Topological data analysis in biomedicine: A review,” *Journal of Biomedical Informatics*, vol. 130, p. 104082, 2022.
- [26] G. Carlsson and M. Vejdemo-Johansson, *Topological data analysis with applications*. Cambridge University Press, 2021.
- [27] C. M. Pereira and R. F. de Mello, “Persistent homology for time series and spatial data clustering,” *Expert Systems with Applications*, vol. 42, no. 15-16, pp. 6026–6038, 2015.
- [28] U. Islambekov and Y. R. Gel, “Unsupervised space–time clustering using persistent homology,” *Environmetrics*, vol. 30, no. 4, p. e2539, 2019.
- [29] E. Tan, S. Algar, D. Corrêa, M. Small, T. Stemler, and D. Walker, “Selecting embedding delays: An overview of embedding techniques and a new method using persistent homology,” *Chaos: An Interdisciplinary Journal of Nonlinear Science*, vol. 33, no. 3, 2023.
- [30] F. A. Khasawneh and E. Munch, “Stability determination in turning using persistent homology and time series analysis,” in *ASME International Mechanical Engineering Congress and Exposition*, vol. 46483, p. V04BT04A038, American Society of Mechanical Engineers, 2014.
- [31] H. Abdallah, A. Regalski, M. B. Kang, M. Berishaj, N. Nnadi, A. Chowdury, V. A. Diwadkar, and A. Salch, “Statistical inference for persistent homology applied to simulated fmri time series data,” *Foundations of Data Science*, vol. 5, no. 1, pp. 1–25, 2023.
- [32] M. Flammer, “Persistent homology-based classification of chaotic multi-variate time series: application to electroencephalograms,” *SN Computer Science*, vol. 5, no. 1, p. 107, 2023.

- [33] P. Lawson, A. B. Sholl, J. Q. Brown, B. T. Fasy, and C. Wenk, “Persistent homology for the quantitative evaluation of architectural features in prostate cancer histology,” *Scientific reports*, vol. 9, no. 1, p. 1139, 2019.
- [34] G. Tauzin, U. Lupo, L. Tunstall, J. B. Pérez, M. Caorsi, A. M. Medina-Mardones, A. Dassatti, and K. Hess, “giotto-tda:: A topological data analysis toolkit for machine learning and data exploration,” *Journal of Machine Learning Research*, vol. 22, no. 39, pp. 1–6, 2021.
- [35] U. Bauer, “Ripser: efficient computation of vietoris–rips persistence barcodes,” *Journal of Applied and Computational Topology*, vol. 5, no. 3, pp. 391–423, 2021.
- [36] C. Maria, J.-D. Boissonnat, M. Glisse, and M. Yvinec, “The gudhi library: Simplicial complexes and persistent homology,” in *Mathematical Software–ICMS 2014: 4th International Congress, Seoul, South Korea, August 5–9, 2014. Proceedings 4*, pp. 167–174, Springer, 2014.
- [37] K. Combs and T. Bihl, “Clustering and topological data analysis: Comparison and application,” 2023.
- [38] R. Nishino and S. H. C. Loomis, “Cupy: A numpy-compatible library for nvidia gpu calculations,” *31st conference on neural information processing systems*, vol. 151, no. 7, 2017.
- [39] A. H. Bermano, R. Gal, Y. Alaluf, R. Mokady, Y. Nitzan, O. Tov, O. Patashnik, and D. Cohen-Or, “State-of-the-art in the architecture, methods and applications of stylegan,” in *Computer Graphics Forum*, vol. 41, pp. 591–611, Wiley Online Library, 2022.
- [40] A. Voulodimos, N. Doulamis, A. Doulamis, and E. Protopapadakis, “Deep learning for computer vision: A brief review,” *Computational intelligence and neuroscience*, vol. 2018, no. 1, p. 7068349, 2018.
- [41] A. Creswell, T. White, V. Dumoulin, K. Arulkumaran, B. Sengupta, and A. A. Bharath, “Generative adversarial networks: An overview,” *IEEE signal processing magazine*, vol. 35, no. 1, pp. 53–65, 2018.
- [42] S. Grossberg, “Recurrent neural networks,” *Scholarpedia*, vol. 8, no. 2, p. 1888, 2013.
- [43] M. Krithika Alias AnbuDevi and K. Suganthi, “Review of semantic segmentation of medical images using modified architectures of unet,” *Diagnostics*, vol. 12, no. 12, p. 3064, 2022.
- [44] Y. LeCun, Y. Bengio, and G. Hinton, “Deep learning,” *nature*, vol. 521, no. 7553, pp. 436–444, 2015.
- [45] H. Zhou, S. Zhang, J. Peng, S. Zhang, J. Li, H. Xiong, and W. Zhang, “Informer: Beyond efficient transformer for long sequence time-series forecasting,” in *Proceedings of the AAAI conference on artificial intelligence*, vol. 35, pp. 11106–11115, 2021.
- [46] A. Zomorodian, “Fast construction of the vietoris–rips complex,” *Computers & Graphics*, vol. 34, no. 3, pp. 263–271, 2010.
- [47] L. J. Guibas, Q. Mérigot, and D. Morozov, “Witnessed k-distance,” in *Proceedings of the twenty-seventh annual symposium on Computational geometry*, pp. 57–64, 2011.
- [48] R. Charney, “An introduction to right-angled artin groups,” *Geometriae Dedicata*, vol. 125, pp. 141–158, 2007.

- [49] S. Dantchev and I. Ivrissimtzis, “Efficient construction of the čech complex,” *Computers & Graphics*, vol. 36, no. 6, pp. 708–713, 2012.
- [50] D. Cohen-Steiner, H. Edelsbrunner, and J. Harer, “Stability of persistence diagrams,” in *Proceedings of the twenty-first annual symposium on Computational geometry*, pp. 263–271, 2005.
- [51] P. Bubenik, “The persistence landscape and some of its properties,” in *Topological Data Analysis: The Abel Symposium 2018*, pp. 97–117, Springer, 2020.
- [52] Z. Cang, L. Mu, K. Wu, K. Opron, K. Xia, and G.-W. Wei, “A topological approach for protein classification,” *Computational and Mathematical Biophysics*, vol. 3, no. 1, 2015.
- [53] A. Adcock, E. Carlsson, and G. Carlsson, “The ring of algebraic functions on persistence bar codes,” *arXiv preprint arXiv:1304.0530*, 2013.
- [54] S. Kališnik, “Tropical coordinates on the space of persistence barcodes,” *Foundations of Computational Mathematics*, vol. 19, no. 1, pp. 101–129, 2019.
- [55] X. Zhu, “Persistent homology: An introduction and a new text representation for natural language processing.,” in *IJCAI*, no. 2013, pp. 1953–1959, 2013.
- [56] B. Zieliński, M. Lipiński, M. Juda, M. Zeppelzauer, and P. Dłotko, “Persistence codebooks for topological data analysis,” *Artificial Intelligence Review*, vol. 54, pp. 1969–2009, 2021.
- [57] I. Goodfellow, J. Pouget-Abadie, M. Mirza, B. Xu, D. Warde-Farley, S. Ozair, A. Courville, and Y. Bengio, “Generative adversarial networks,” *Communications of the ACM*, vol. 63, no. 11, pp. 139–144, 2020.
- [58] G. Papamakarios, E. Nalisnick, D. J. Rezende, S. Mohamed, and B. Lakshminarayanan, “Normalizing flows for probabilistic modeling and inference,” 2021.
- [59] Y. Dukler, W. Li, A. Lin, and G. Montúfar, “Wasserstein of wasserstein loss for learning generative models,” in *International conference on machine learning*, pp. 1716–1725, PMLR, 2019.
- [60] X. Mao, Q. Li, H. Xie, R. Y. Lau, Z. Wang, and S. Paul Smolley, “Least squares generative adversarial networks,” in *Proceedings of the IEEE international conference on computer vision*, pp. 2794–2802, 2017.
- [61] O. Mogren, “C-rnn-gan: Continuous recurrent neural networks with adversarial training,” *arXiv preprint arXiv:1611.09904*, 2016.
- [62] R. B. Arantes, G. Vogiatzis, and D. R. Faria, “Rcgan: learning a generative model for arbitrary size image generation,” in *Advances in Visual Computing: 15th International Symposium, ISVC 2020, San Diego, CA, USA, October 5–7, 2020, Proceedings, Part I 15*, pp. 80–94, Springer, 2020.
- [63] Y. Zhang, Z. Zhou, J. Liu, and J. Yuan, “Data augmentation for improving heating load prediction of heating substation based on timegan,” *Energy*, vol. 260, p. 124919, 2022.
- [64] K. H. D. Tang, “Climate change in malaysia: Trends, contributors, impacts, mitigation and adaptations,” *Science of the Total Environment*, vol. 650, pp. 1858–1871, 2019.
- [65] S. Elfwing, E. Uchibe, and K. Doya, “Sigmoid-weighted linear units for neural network function approximation in reinforcement learning,” *Neural networks*, vol. 107, pp. 3–11, 2018.

- [66] J. Song, C. Meng, and S. Ermon, “Denoising diffusion implicit models,” *arXiv preprint arXiv:2010.02502*, 2020.
- [67] D. Kingma, T. Salimans, B. Poole, and J. Ho, “Variational diffusion models,” *Advances in neural information processing systems*, vol. 34, pp. 21696–21707, 2021.
- [68] P. Dhariwal and A. Nichol, “Diffusion models beat gans on image synthesis,” *Advances in neural information processing systems*, vol. 34, pp. 8780–8794, 2021.
- [69] P. Handel, “Parameter estimation employing a dual-channel sine-wave model under a gaussian assumption,” *IEEE Transactions on Instrumentation and Measurement*, vol. 57, no. 8, pp. 1661–1669, 2008.
- [70] L. Van der Maaten and G. Hinton, “Visualizing data using t-sne.,” *Journal of machine learning research*, vol. 9, no. 11, 2008.
- [71] J. Lee, D. Jung, J. Moon, and S. Rho, “Advanced r-gan: Generating anomaly data for improved detection in imbalanced datasets using regularized generative adversarial networks,” *Alexandria Engineering Journal*, vol. 111, pp. 491–510, 2025.
- [72] Y. Lu and J. Lu, “A universal approximation theorem of deep neural networks for expressing probability distributions,” *Advances in neural information processing systems*, vol. 33, pp. 3094–3105, 2020.
- [73] L. Dinh, J. Sohl-Dickstein, and S. Bengio, “Density estimation using real nvp,” *arXiv preprint arXiv:1605.08803*, 2016.
- [74] G. Papamakarios, T. Pavlakou, and I. Murray, “Masked autoregressive flow for density estimation,” *Advances in neural information processing systems*, vol. 30, 2017.
- [75] H. J. Van Veen, N. Saul, D. Eargle, and S. W. Mangham, “Kepler mapper: A flexible python implementation of the mapper algorithm.,” *Journal of Open Source Software*, vol. 4, no. 42, p. 1315, 2019.

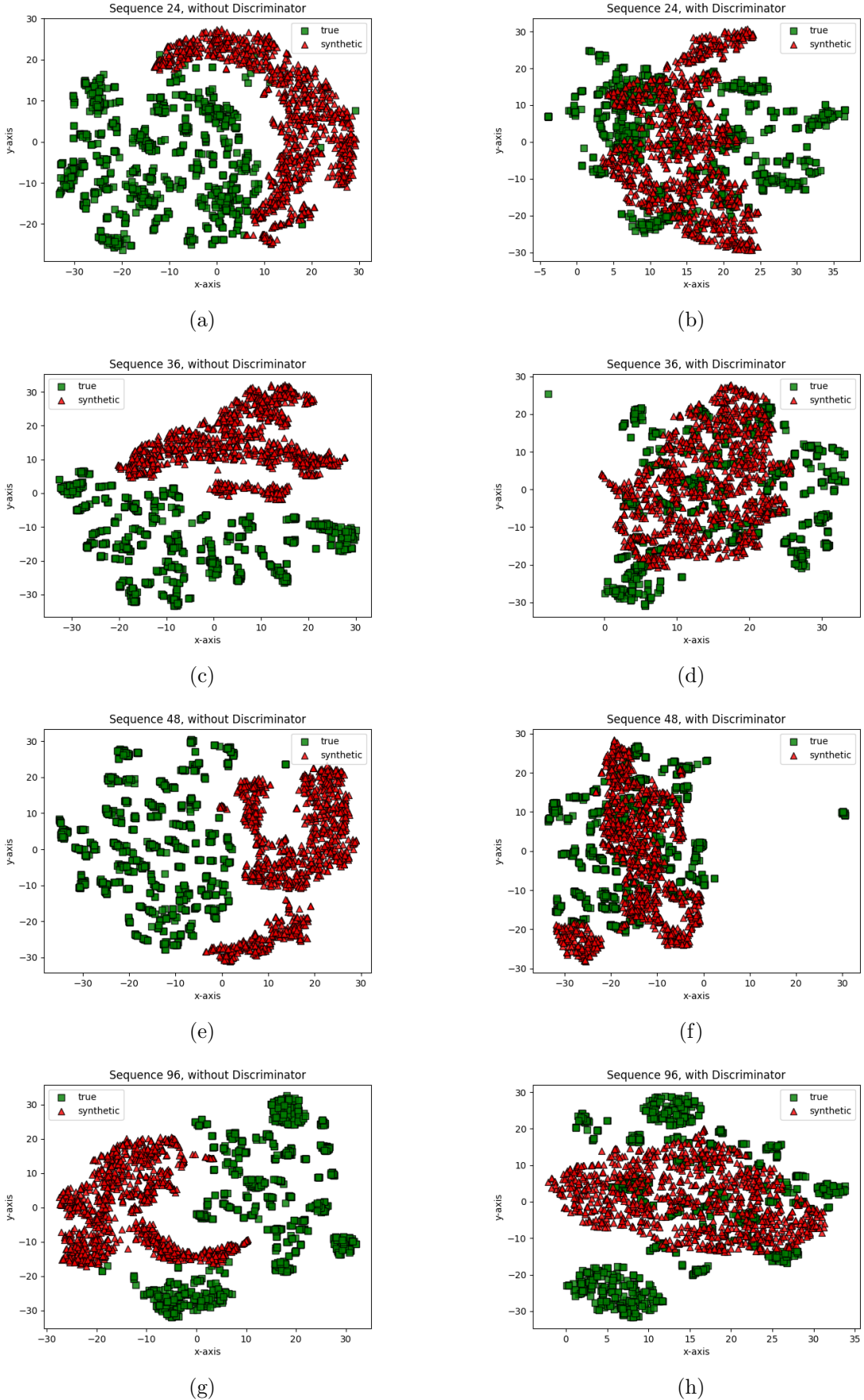


Figure 13: t-SNE visualizations comparing true (green squares) and synthetic (red triangles) topological features for different sequence lengths.